Characterizing the Influence of Fracture Density on Network Scale Transport

Thomas Sherman[1], Jeffrey Hyman[2], Marco Dentz[3], Diogo Bolster[1]

[1]Department of Civil and Environmental Engineering and Earth Sciences, University of Notre Dame, Notre Dame, IN, USA

[2]Computational Earth Science Group(EES-16), Earth and Environmental Sciences Division, Los Alamos National Laboratory, Los Alamos, NM 87545

[3]Spanish National Research Council (IDAEA-CSIC), Barcelona, Spain

Key Points:

- We investigate the impact of fracture density on transport in three-dimensional fracture networks
- Negative velocity zones influence network scale transport behavior
- A tortuosity dependent Bernoulli CTRW model is used to upscale topological heterogeneity

Corresponding author: Thomas Sherman, `tsherma3@nd.edu`

Abstract

The topology of natural fracture networks is inherently linked to the structure of the fluid velocity field and transport therein. Here we study the impact of network density on flow and transport behaviors. We stochastically generate fracture networks of varying density and simulate flow and transport with a high fidelity Discrete Fracture Network (DFN) model, that fully resolves network topology at the fracture scale. We study conservative solute trajectories in great detail with Lagrangian particle tracking and find that as fracture density decreases, solute channelization to large local fractures increases, thereby reducing solute plume spreading. Furthermore, in sparse networks mean particle travel distance increases and local network features, such as negative velocity zones, become increasingly important for transport. As the network density increases, network statistics homogenize and such local features have a reduced impact. We quantify local topological influence on transport behavior with an effective tortuosity parameter, which measures the ratio of total advective distance to linear distance at the fracture scale; large tortuosity values are correlated to slow velocity regions. These large tortuosity - slow velocity regions delay downstream transport and enhance tailing on particle breakthrough curves. Finally, we predict transport with an upscaled, Bernoulli spatial Markov random walk model and parameterize local topological influences with a novel tortuosity parameter. Bernoulli model predictions improve when sampling from a tortuosity distribution, as opposed to a fixed value as has previously been done, suggesting that local network topological features must be carefully considered in upscaled modelling efforts of fracture network systems.

1 Introduction

In subsurface low permeability rocks, fractures form complex networks that control fluid flow and transport of dissolved solutes and other compounds. The inherent heterogeneous structure of natural fracture networks is characterized by a broad range of lengths, spanning from the aperture roughness to the full network scale (Bonnet et al., 2001). At the network scale, the topological properties set the flow field structure (de Dreuzy et al., 2012; Frampton et al., 2019; Makedonska et al., 2016), meaning velocity at the in-fracture scale is highly correlated (Kang, Le Borgne, et al., 2015; J. Hyman et al., 2019) and sub fracture scale features are less important. Complex network topologies naturally result in a very broadly distributed velocity field, which influences associated transport processes. Specifically, this broad distribution manifests in anomalous transport, i.e. transport which cannot be adequately described with an upscaled effective Fickian advection dispersion equation (ADE) (Cushman, 2013; Le Borgne et al., 2008a; Dentz & Bolster, 2010; Becker & Shapiro, 2000, 2003; Kang, Le Borgne, et al., 2015); anomalous characteristics can be observed on concentration breakthrough curves and include early arrival of tracer and enhanced late time breakthrough tailing. Hence, accurately parameterizing network topology in transport models remains critical for many applications of scientific and practical interest, including CO_2 sequestration (Pacala & Socolow, 2004), geothermal energy (Barbier, 2002) and hydrocarbon extraction (J. D. Hyman, Jiménez-Martínez, et al., 2016).

Discrete fracture network (DFN) models are a common method for simulating flow and transport through fractured media (Cacas et al., 1990; de Dreuzy et al., 2004; Bogdanov et al., 2007). Recent advances in computational technologies have enabled simulation of three-dimensional (3D) DFNs, where the network structure, and features such as local circulation zones (Park et al., 2003), which are not possible in 2D representations, can be studied in detail. In the DFN approach, fractures are explicitly represented as lower dimensional structures, enabling accurate representation of the network structure, e.g., geometry and topology, and the corresponding flow field. The flow field within an individual fracture is typically highly correlated, commonly causing solute velocity to display persistent, low variability behavior over the in-fracture scale; consequently, the greatest Lagrangian accelerations occur at fracture intersections (Kang, Le Borgne, et al., 2015; J. Hyman et al., 2019). As the fracture density increases, solute encounters more intersections on average and the velocity correlation scale decreases. Furthermore, strong preferential flow paths form within interconnected networks of large fractures and channel a significant portion of mass, enabling solute to persist at high velocities for distances greater than the single fracture scale (Kang, Dentz, et al., 2015; Kang et al., 2019). This channelization becomes enhanced in sparse networks, where particles encounter fewer intersections, enabling them to persist on single fractures for longer distances. Resolving all these intra-network features in 3D DFN models is still computationally costly, and so upscaled modeling approaches, which account for network variability through effective parameter schemes, while maintaining a parsimonious framework, present an attractive alternative. However, how to properly parameterize network properties, such as velocity correlation and geometry, and incorporate them properly into such effective upscaled models remains an open challenge and area of active research.

Continuous time random walk (CTRW) and time domain random walk (TDRW) models (Berkowitz et al., 2006; Noetinger et al., 2016) provide natural frameworks to upscale transport in media with spatially variable flow properties (Berkowitz & Scher, 1997; S. Painter & Cvetkovic, 2005; Dentz et al., 2016; Comolli & Dentz, 2017; Puyguiraud et al., 2019b). In these approaches, a solute plume is conceptualized as an assembly of idealized solute particles who transition through time and space by sampling the local flow velocities. The velocity series sampled along a particle trajectory is modeled as spatial Markov processes of uncorrelated (Berkowitz & Scher, 1997; Berkowitz et al., 2006) or correlated subsequent velocities (Le Borgne et al., 2008a, 2008b; Kang et al., 2011; Bolster et al., 2014; Dentz et al., 2016; Morales et al., 2017; Sherman et al., 2018). The velocity Markov chain is characterized by a transition matrix, which characterizes how solute velocity transitions over fixed spatial increments, and has been demonstrated to accurately capture transport in porous media (Le Borgne et al., 2008b; De Anna et al., 2013; Kang et al., 2014) and fracture networks (Kang et al., 2011; Kang, Le Borgne, et al., 2015; Kang, Dentz, et al., 2015; Kang et al., 2016). The transition matrix can be determined empirically by sampling velocity transitions along particle trajectories (Le Borgne et al., 2008b), inverse modelling algorithms applied to experimental concentration profiles (Sherman et al., 2017, 2018), or by parametric models given by analytical Markov models (Kang, Le Borgne, et al., 2015; Kang, Dentz, et al., 2015; Dentz et al., 2016; Morales et al., 2017; Hakoun et al., 2019). Here we focus on the CTRW implementation that models the series of particle velocity magnitudes as a Bernoulli process, (Dentz et al., 2016; Holzner et al., 2015; Massoudieh et al., 2017; Carrel et al., 2018; J. Hyman et al., 2019; Puyguiraud et al., 2019a, 2019b; Kang et al., 2019), meaning a particle's speed persists from the previous step if a weighted coin lands heads and is re-sampled if it lands tails. This probability is often found by assuming velocity transitions at a constant rate, inversely proportional to a correlation distance (Dentz et al., 2016; J. Hyman et al., 2019). In this framework, particle motion along a tortuous pathline is projected onto streamwise distance using the concept of tortuosity, which measures the ratio between the average trajectory length and streamwise distance (Koponen et al., 1996; Ghanbarian et al., 2013). However, heterogeneity of the network enables particles to experience a distribution of trajectory lengths, which is not accounted for by an average tortuosity value.

In this paper, we use high-fidelity numerical simulations of flow and transport through 3D DFNs to study the influence of fracture density on transport behavior. All other network attributes are kept constant across the different network realizations. We observe that in sparse networks, single fractures become increasingly important, resulting in enhanced flow channelization and reduced spreading of the solute plume. Furthermore, we observe that the mean advective travel distance from inlet to outlet increases with decreasing density. In all networks, the local effective tortuosity is broadly distributed and related to low velocity regions, which in turn give rise to late time tailing in network scale breakthrough curves. Hence network topology and density play an important role in network scale transport. We capture local topological effects in the CTRW framework by sampling from a tortuosity distribution as well as sampling from a tortuosity-velocity joint distribution. We compare the upscaled model performance against high fidelity DFN simulations. The proposed CTRW implementation provides insights on the relationship between local topological effects and network scale transport behavior.

2 Numerical Simulations

In this section, we describe our modeling methodology for simulating and analyzing flow and transport in subsurface fracture networks.

2.1 Discrete Fracture Networks

We use the high-fidelity three-dimensional discrete fracture network modeling suite dfnWorks (J. D. Hyman, Karra, et al., 2015) to generate each DFN, solve the steady-state flow equations and simulate transport therein using particle tracking. dfnWorks combines the feature rejection algorithm for meshing (fram) (J. D. Hyman et al., 2014), the LaGriT meshing toolbox (LaGriT, 2013), the parallelized subsurface flow and reactive transport code pflotran (Lichtner et al., 2015), and an extension of the walkabout particle tracking method (Makedonska et al., 2015; S. L. Painter et al., 2012). fram is used to generate three-dimensional fracture networks. LaGriT is used to create a computational mesh representation of the DFN in parallel. pflotran is used to numerically integrate the governing flow equations. walkabout is used to determine pathlines through the DFN and simulate solute transport. Details of the suite, its abilities, applications, and references for detailed implementation are provided in J. D. Hyman, Karra, et al. (2015).

2.1.1 Network Generation

Fractures are represented as planar discs whose radii r are sampled from a truncated power law distribution with upper and lower cutoffs (r_u; r_0) and exponent α:

$$p_r(r) = \frac{\alpha}{r_0} \frac{(r/r_0)^{-1-\alpha}}{1-(r_u/r_0)^{-\alpha}}. \tag{1}$$

We consider an exponent of 1.8, a lower cut off of 1 m and upper cut off of 10 m. We non-dimensionalize length scales by the minimum fracture size r_0; $r' = r/r_0$. Each DFN is generated in a cubic domain with sides of dimensionless length 50. Fracture apertures are positively correlated to the fracture radii via a power-law relationship

$$b = \gamma r^{\beta}, \tag{2}$$

where $\beta = 0.5$ [-] and $\gamma = 5.0\times10^{-4}$ $[L^{1-\beta}]$ are parameters based on field data (Svensk Kärnbränslehantering AB, 2010). This correlation between fracture size and aperture is a common assumption in DFN models (Bogdanov et al., 2007; de Dreuzy et al., 2002; Frampton & Cvetkovic, 2010; J. D. Hyman, Aldrich, et al., 2016; Joyce et al., 2014; Wellman et al., 2009).

We consider a single fracture family whose centers are uniformly distributed throughout the domain. The domain is slightly enlarged during the generation phase, and then reduced to the 50 meter cube once target densities have been achieved. This procedure limits boundary effects near the edge of the domain, where otherwise non-uniform densities occur. The orientations of fractures follow a Fisher distribution,

$$f(\mathbf{x};\boldsymbol{\mu},\kappa) = \frac{\kappa \exp(\kappa \boldsymbol{\mu}^T \mathbf{x})}{4\pi \sinh(\kappa)}, \tag{3}$$

sampled using Wood's algorithm (Wood, 1994). In (3), $\boldsymbol{\mu}$ is the mean direction vector, which can be expressed in terms of spherical coordinates, θ and ϕ, and $\kappa \geq 0$ is the concentration parameter that determines the degree of clustering around the mean direction. Values of κ approaching zero represent a uniform distribution on the sphere while larger values generate small average deviations from the mean direction. We set $\kappa = 0.1$ so that fracture orientations are uniformly random; it is a disordered network, which means there is not preferred direction of flow due to fracture orientation.

We generate three sets of networks, each with a different density. Density of the fractures networks is measured using a dimensionless version of the percolation parameter p defined by de Dreuzy, Davy, and Bour (2000). The dimensionless form is $p' = p/p_c$, where p_c is the critical percolation density value (the minimum number of fractures) such that there is almost surely a connected cluster of fractures than spans the whole domain (Berkowitz & Balberg, 1993; Bour & Davy, 1997, 1998; Sahimi, 1994). An advantage of p' is that it provides a constant measure of density with respect to the percolation threshold (de Dreuzy et al., 2012). For the domain size and truncated power law distribution parameters, $p_c = 766$ fractures, we select three dimensionless densities, $p' = 3$, $p' = 5$, and $p' = 10$. We generate 10 independent networks at each density. Figure 1 shows one sample from each of the sets. On the left is one network from the $p' = 3$ samples, in the middle is a network from the $p' = 5$ samples, and one network from the $p' = 10$ samples is shown in the right sub-figure. Fractures are colored by their radius, which ranges from $r' = 1$ to $r' = 10$.

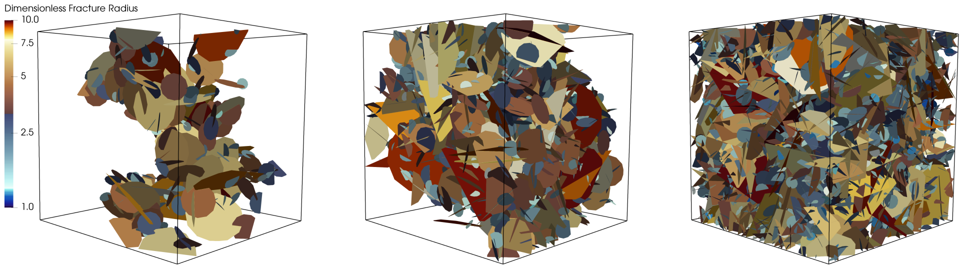

Figure 1. One DFN sample from each of the sets (left) $p' = 3$, (middle) $p' = 5$, and (right) $p' = 10$. Fractures are colored by their size, with larger fractures having warmer colors.

2.1.2 Network Characterization

The selected densities result in networks with different geometric and topological properties. Table 1 reports the requested number of fractures to achieve target densities along with the final number in the network used for flow simulation. Fractures that are part of a cluster that do not connect between inflow and outflow boundaries, and therefore do not contribute to flow and transport through the medium, are removed from the domain after generation. As the density increases, the difference between the requested and final number of fractures, i.e. the number of fractures removed from the domain relative to the requested value, decreases, indicating that the networks are better connected at higher density.

We measure the network connectivity using a graph-based approach (J. D. Hyman et al., 2018; Huseby et al., 1997), where vertices in the graph correspond to fractures in the DFN and there is an edge between those vertices if the corresponding fractures intersect in the DFN. We augment the graph to include source and target vertices, corresponding to the inflow and outflow boundaries, and provide a topological point of reference with respect to inflow and outflow boundaries within the graph. For every fracture that intersects the inflow boundary, an edge is added between the vertex in the graph corresponding to that fracture and the vertex representing the inflow boundary; likewise for the outflow boundary. Similar graph-theoretical approaches have been used for a variety of studies concerning fractured media including topological characterization of networks (Andresen et al., 2013; Hope et al., 2015; Huseby et al., 1997; J. D. Hyman & Jiménez-Martínez, 2018) and backbone identification (Aldrich et al., 2017; J. D. Hyman et al., 2017; Rizzo & de Barros, 2017; Valera et al., 2018). The utility of this graph-based approach is that topological properties of the networks can be queried and characterized in a formal mathematical framework while retaining physical interpretation.

We begin with local topological attributes of the networks and a specific focus on the number of intersections on each fracture, which we refer to as the *fracture degree* and denote as d. Within the context of our graph representation, this value is the degree of corresponding nodes in the graph. The mean of the distribution of fracture degree $\bar{d}$ is another definition of dimensionless density detailed in (Mourzenko et al., 2005) and is provided in Table 1. The observed mean values are relatively close to one another, ≈ 2 with slightly higher values observed at higher densities. We also include the variance of the degree distributions to show that the range of fracture degrees in the networks broadens as density increases. Physically, these values indicate that a typical fracture connects to 2-3 other fractures in all networks, but as the density of the network increases there are more fractures with many intersections. The degree of a fracture is positively correlated to fracture radius, with a correlation coefficient of ≈ 0.8 for all networks. Hence, larger fractures are better connected than smaller ones, which is a result of individual fracture geometry. Recall, that the distributions of fracture radii follow a power-law distribution, which implies that there are numerous small fractures with few connections along with fewer large ones with many intersections. However, these observations do not inform us if larger fractures are connected to numerous larger fractures or to smaller ones. To explore this, we can compute the assortativity coefficient $\mathcal{P}$ of the sets, quantified using the Pearson correlation coefficient (Newman, 2002, 2003), which ranges between -1 and 1. Values greater than 0 indicate correlation between vertices of similar degree, while values less than 0 indicate correlation between vertices of different degrees. In all cases, the value is less than 0, which indicates the networks exhibit disassortative mixing. There is a slight correlation between the density and $\mathcal{P}$, where higher density results to less disassortativity. In combination, these values show that well-connected larger fractures intersect with smaller fractures that have fewer intersections.

We also investigate one global topological quantity that measures the robustness of the network. The node connectivity of a graph (n_c) is the fewest number of nodes that needs to be removed from a network to disconnect source and target. In terms of the DFN, it is the fewest number of fractures that need to be removed to disconnect inflow and outflow boundaries. For the lowest density sets, the average n_c is close to 1 indicating that the flow must channelize through a single fracture being constrainted by the network structure. In contrast, the highest density set has an average of close to 30, which means that flow through that network will be far less constrained by the network structure. In conjunction, these values indicate that the higher density networks are much better connected than the lower density ones.

In the next section, we describe flow and transport simulations in these networks and discuss how these structural properties influence the flow field therein.

Table 1. Network Characterization: Number of Fractures (# F), Dimensionless connected network density p', Mean fracture degree $\bar{d}$, Variance of fracture degree $\sigma(d)$, assortativity coefficient $\mathcal{P}$, node connectivity n_c

Set	p′	# F	# $\hat{\text{F}}$ (Nonisolated)	$\bar{d}$	$\sigma(d)$	$\mathcal{P}$	n_c
P3	3	2300	220.10 (±87.46)	2.20 (±0.06)	3.50 (±0.41)	-0.26 (±0.06)	1.20 (±0.40)
P5	5	3600	1339.90 (±130.13)	2.32 (±0.03)	4.93 (±0.22)	-0.18 (±0.03)	6.90 (±1.30)
P10	10	7600	4069.30 (±46.32)	2.65 (±0.03)	9.77 (±0.47)	-0.12 (±0.01)	29.60 (±2.97)

2.2 Flow and Transport Simulation

In the DFN methodology there is no interaction between flow within the fractures and the surrounding matrix. We consider the flow of a Newtonian fluid, in our case water, at Reynolds number $Re < O(1)$ and thus assume Stokes flow within each fracture. Mass conservation along with Darcy's equation, which governs momentum, are used to form an elliptic partial differential equation for the steady-state distribution of pressure within the network

$$\nabla \cdot \left(b^3(\mathbf{x})\nabla P\right) = 0 \ , \tag{4}$$

where b is the fracture aperture, which is uniform within a fracture but varies between fractures, cf. (2), and ∇P is the local pressure gradient. Flow through each network is created by applying a pressure difference of 1 MPa across the domain along the x-axis and no-flow boundary conditions are applied along lateral boundaries. For simplicity, the effects of gravity are not considered in these simulations. Equation (4) is numerically integrated using a two-point flux finite-volume scheme implemented in PFLOTRAN that ensures local mass conservation within fracture planes and at fracture intersections to obtain pressure values and volumetric fluxes throughout the domain. The Eulerian velocity field $\mathbf{u}(\mathbf{x})$ is reconstructed using obtained values of pressures P and volumetric flow rates (Makedonska et al., 2015; S. L. Painter et al., 2012) which is spatially variable within each plane. Also, we consider the distribution of velocity magnitude $v_e(\mathbf{x}) = \|\mathbf{u}(\mathbf{x})\|$ throughout the entire domain, i.e. the Eulerian velocity distribution is defined as

$$\psi_e(v) = \frac{1}{V_e}\int\limits_{\Omega_e} d\mathbf{x}\delta[v - v_e(\mathbf{x})], \tag{5}$$

where Ω_e is the flow domain and V_e its volume.

The transport of a nonreactive conservative solute plume through each network is simulated using an ensemble of purely advective particles, denoted as Ω. The pressure gradient is imposed along the x axis, and therefore the primary flow direction is also along the x axis. The initial positions of particles ($\mathbf{a}$) along the inlet plane $x = 0$ are determined using a flux-weighted injection condition so that the number of particles is proportional to the local incoming volumetric flow rate (Kreft & Zuber, 1978; Frampton & Cvetkovic, 2009; J. D. Hyman, Painter, et al., 2015). The trajectory $\mathbf{x}(t;\mathbf{a})$ of a particle starting at $\mathbf{a}$ at time $t = 0$ is given by the advection equation

$$\frac{d\mathbf{x}(t;\mathbf{a})}{dt} = \mathbf{v}_t(t;\mathbf{a}), \qquad\qquad \mathbf{x}(0;\mathbf{a}) = \mathbf{a}, \tag{6}$$

where the Lagrangian velocity $\mathbf{v}_t(t;\mathbf{a})$ is given by the Eulerian velocity $\mathbf{u}(\mathbf{x})$

$$\mathbf{v}_t(t;\mathbf{a}) = \mathbf{u}[\mathbf{x}(t;\mathbf{a})]. \tag{7}$$

At fracture intersections, we adopt a complete mixing rule, which means that the probability to exit an outgoing fracture is determined by the flux (Kang, Dentz, et al., 2015; Sherman et al., 2019).

The length $\ell(t;\mathbf{a})$ of the trajectory at a time t is given by

$$\frac{d\ell(t;\mathbf{a})}{dt} = v_t(t,\mathbf{a}). \tag{8}$$

where the Lagrangian velocity magnitude is $v_t(t,\mathbf{a}) = |\mathbf{v}_t(t,\mathbf{a})|$. The pathline length, ℓ, is used to parameterize the spatial and temporal coordinates of the particle. In terms of ℓ, the space-time particle trajectory is

$$\frac{d\mathbf{x}(\ell;\mathbf{a})}{d\ell} = \frac{\mathbf{v}_\ell(\ell;\mathbf{a})}{v_\ell(\ell;\mathbf{a})} \tag{9a}$$

$$\frac{dt(\ell;\mathbf{a})}{d\ell} = \frac{1}{v_\ell(\ell,\mathbf{a})} \tag{9b}$$

where the space-Lagragian velocity is $\mathbf{v}_\ell(\ell,\mathbf{a}) = \mathbf{u}[\mathbf{x}(\ell;\mathbf{a})]$ and its magnitude $v_\ell(\ell,\mathbf{a}) = |\mathbf{v}_\ell(\ell,\mathbf{a})|$.

Across each ensemble of M particles, denoted Ω_a, we compute the distribution of velocities, correlation of velocity along pathlines, and tortuosity. The distribution of the Lagrangian velocity magnitude $v_\ell(\ell)$ sampled equidistantly at very fine spatial increments along pathlines is given by

$$\hat{\psi}_\ell(v,\ell) = \frac{1}{M}\int\limits_{\Omega_a} d\mathbf{a}\delta[v - v_\ell(\ell,\mathbf{a})], \tag{10}$$

which we refer to as space Lagrangian.

We also calculate properties of particles at successive control planes x_i perpendicular to the primary flow direction and equally spaced with distance $\Delta l = 1$. Note here the sampling frequency is much coarser than the one used in the equation 10. The distribution of velocities sampled by particles at these control planes is given by

$$\psi_l(v,x_i) = \frac{1}{M}\int\limits_{\Omega_a} d\mathbf{a}\delta[v - v_\ell(x_i,\mathbf{a})]\ . \tag{11}$$

The PDF of velocity magnitudes in the injection domain is given by $\psi_0(v) = \hat{\psi}_\ell(v,\ell = 0)$, which corresponds to our flux-weighted initial conditions and relates the $\psi_l(v,x_1)$ to

$\psi_e(v)$. We primarily consider a global Lagrangian velocity distribution $\psi_l(v)$ that is the aggregate of $\psi_l(v, x_1)$ across all control planes.

We define the first arrival time $\tau(x_i; \mathbf{a})$ of a particle at a control plane located at x_i to be

$$\tau(x_i; \mathbf{a}) = t[\lambda(x_i, \mathbf{a}); \mathbf{a}], \qquad \lambda(x_i, \mathbf{a}) = \inf\{\ell | x_i(\ell; \mathbf{a}) \geq x_i\}. \tag{12}$$

At each control plane, individual particle breakthrough times are combined to provide the distribution of first passages times across the ensemble

$$\Psi(t; x_i) = \frac{1}{M} \int\limits_{\Omega_a} d\mathbf{a} H[t - \tau(x_i; \mathbf{a})] \tag{13}$$

which we call the breakthrough curve. Here $H(t)$ is the Heaviside function and equation 13 is the CDF of solute first passage times at a control plane.

Additionally, we measure tortuosity statistics. A search of the literature reveals various definitions of tortuosity, e.g. geometric, hydraulic, and electrical, all of which have been used to study different subsurface properties, i.e. subsurface structure, conductivity, solute travel time, and solute dispersion (Ghanbarian et al., 2013). In this study, we focus on a flow-dependent tortuosity, as it is naturally compatible with Lagrangian observations. We define an effective tortuosity between two control planes at x_i and x_j ($x_j < x_i$) as the pathline distance traveled by a particle between the control planes $\Delta\ell_{i,j}(\mathbf{a}) = |\lambda(x_i; \mathbf{a}) - \lambda(x_j; \mathbf{a})|$ divided by the linear distance between those control planes $\Delta x_{i,j} = |x_i - x_j|$

$$\chi(x_{i,j}; \mathbf{a}) = \frac{\Delta\ell_{i,j}(\mathbf{a})}{\Delta x_{i,j}} \ . \tag{14}$$

Note with this definition, particles are permitted to leave the observation window via backflow in the DFN, i.e. a particle may cross control plane x_j more than once before reaching x_i. The distribution of effective tortuosity across a particle ensemble is

$$\psi(\chi_{i,j}) = \frac{1}{M} \int\limits_{\Omega_a} d\mathbf{a} \delta[\chi_{i,j} - \chi_{i,j}(\mathbf{a})] \ . \tag{15}$$

For most of our analysis we consider $\Delta x = 1$ for all pairs of subsequent control planes and suppress the subscripts, $\chi \to \chi_{i+1,i}$. The conventional definition of flow tortuosity of the ensemble is $\langle \chi(x) \rangle = \langle \chi_{x,0} \rangle$ where x is the linear distance traveled through the domain from the inlet and angled brackets denote an average over the ensemble of particles. Under ergodic conditions, the asymptotic tortuosity is given by (Koponen et al., 1996)

$$\chi_\infty = \lim_{x\to\infty} \langle \chi(x) \rangle = \frac{\langle v_e \rangle}{\langle u_1 \rangle}. \tag{16}$$

This can be understood as follows: under ergodic conditions, the mean arrival time at x_1 is given by $\langle \tau(x) \rangle = x/\langle u_1 \rangle$, where $\langle u_1 \rangle$ is the average Eulerian velocity in the mean flow direction. At the same time, we have that $\langle \tau(x) \rangle = \langle \lambda(x, \mathbf{a}) \rangle / \langle v_e \rangle$. Equating the two gives (16).

In all cases, one hundred thousand particles are injected and tracked through each network. Increasing the number of particles beyond these counts did not influence upscaled quantities of interest.

3 Velocity Field and Particle Trajectory Observations

In this section, we investigate the relationship between network and flow properties, both Eulerian and Lagrangian.

3.1 Eulerian Properties

The fracture intensity [m^{-1}] (total fracture surface area per unit volume), which is commonly referred to as P_{32} (Dershowitz & Herda, 1992) and computed as:

$$P_{32} = \frac{\sum_f \cdot S_f}{V} \tag{17}$$

is a measure of how much surface area is in a domain. In (17), S_f is the fracture surface area and V is the total size of the domain. While P_{32} provides a compact value that can be compared across networks, it is also useful when compared to the amount of the domain that is actively flowing within a single network, which can be measured using the flow channeling density indicator d_Q (Maillot et al., 2016):

$$d_Q = \frac{1}{V} \cdot \frac{(\sum_f \cdot S_f \cdot Q_f)^2}{(\sum_f \cdot S_f \cdot Q_f^2)} \ . \tag{18}$$

In (18) Q_f is the total flow exchanged by a fracture f with its neighbors. Comparing (17) with (18) suggests that d_Q can be thought as a measure of *active* or *flowing* P_{32}. The flow channeling indicator is a measure of the portion of the total surface area where there is significant flow, which can be quantified using the ratio d_Q/P_{32}. Table 2 provides mean values of P_{32}, d_Q, and d_Q/P_{32} for the networks. As the number of fractures in the network increases with prescribed density, so do all of the observed values. The increase of P_{32} is an obvious and direct consequence of increasing the number of fractures in the network. However, increases of d_Q/P_{32} indicates that flow is less channelized with increasing network density. Recall that the higher density networks are better connected, cf. Table 1, which here is seen as a homogenizer of the flow field within the network.

Table 2. Network Characterization: P_{32} [-], Flow Channeling Indicator d_Q, Percentage of the network flowing d_Q/P_{32}

Set	P_{32}	d_Q	d_Q/P_{32}
P3	0.15 ($\pm$0.06)	0.05 ($\pm$0.02)	0.38 ($\pm$0.09)
P5	0.63 ($\pm$0.06)	0.27 ($\pm$0.04)	0.43 ($\pm$0.05)
P10	1.34 ($\pm$0.02)	0.80 ($\pm$0.03)	0.60 ($\pm$0.02)

3.2 Velocity Distributions

Figure 2 displays the mean of the velocity distributions averaged over all realizations for the fluxed weighted $\psi_e(v)$ (crosses), $\hat{\psi}_\ell(v)$ (triangles) and $\psi_l(v)$ (squares) for the each network density with 95% confidence intervals for $\psi_e(v)$ shaded gray. In all cases velocities are normalized by the mean P3 global Lagrangian velocity $\langle v\rangle_l^{P3}$. Under ergodic conditions and for a sufficiently large injection volume and flow domain, the steady space Lagrangian PDF $\psi_\ell(v) = \lim_{\ell\to\infty} \hat{\psi}_\ell(v,\ell)$ and the Eulerian velocity PDFs are related through flux-weighting

$$\psi_\ell(v) = \frac{v\psi_e(v)}{\langle v_e\rangle}\ , \qquad (19)$$

as shown in Dentz et al. (2016); Comolli and Dentz (2017); Kang, Dentz, Le Borgne, Lee, and Juanes (2017). Near the PDF peaks all the distributions are in good agreement. Interestingly, $\psi_l(v)$ displays lower probability values than $\hat{\psi}_\ell(v)$ in the intermediate velocity regime ($[10^{-3}, 10^{-1}]$) for all network densities, suggesting low velocity regions are under sampled with control planes spaced by distance 1 (the minimum fracture radius). As the network density increases, the PDF peak shifts towards higher velocities and mean particle velocity in the direction of primary flow increases. Additionally, the width of the distribution for the flux weighted Eulerian velocity distribution increases as network density decreases; note the P10 network has a sharpened peak relative to the P3 network.

Furthermore, the size of the 95% confidence intervals increase with network sparsity because the associated increased flow channelization means single fractures have greater influence on transport behavior and the effects of such fractures vary significantly across network realizations.

In dense networks, velocity statistics homogenize across realizations because both network connectivity and flow dispersion increase. Notice that PDF peaks of Eulerian and Lagrangian velocity distributions increasingly deviate as network sparsity increases, suggesting that ergodic assumptions become more valid with increasing fracture density. This behavior is expected as increasing fracture density means that the network is more connected and flow is less channelized, i.e. an increased d_Q/P_{32} value, indicating a greater proportion of the domain is sampled by solute particles.

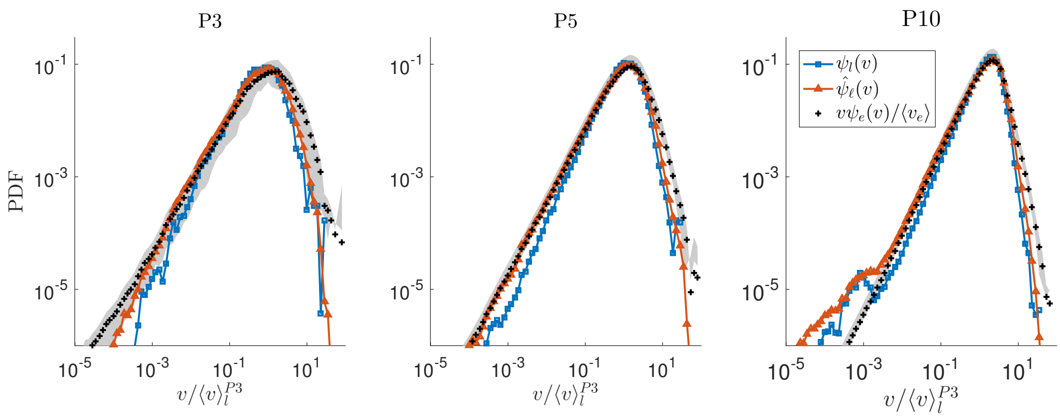

Figure 2. The velocity distributions for each fracture network density averaged over all network realizations. Black crosses are flux-weighted Eulerian, red triangles are the global Langrangian, and blue squares are Lagrangian sampled along control planes. As fracture density increases, the peak of velocity distribution shifts right (increases). Shaded areas show 95% confidence intervals for the Eulerian distributions.

3.3 Tortuosity

The complex geometry of the fracture networks means that the tortuosity distribution is spatially dependent, i.e. transport behavior is dependent on the local topology, which may vary greatly across the network. Figure 3 shows the evolution of the mean tortuosity through space averaged over all realizations. We calculate mean tortuosity at control plane x_i with coordinate x as $\langle \chi(x) \rangle = \langle \lambda(x_i; \mathbf{a})/x \rangle$. The mean tortuosity has

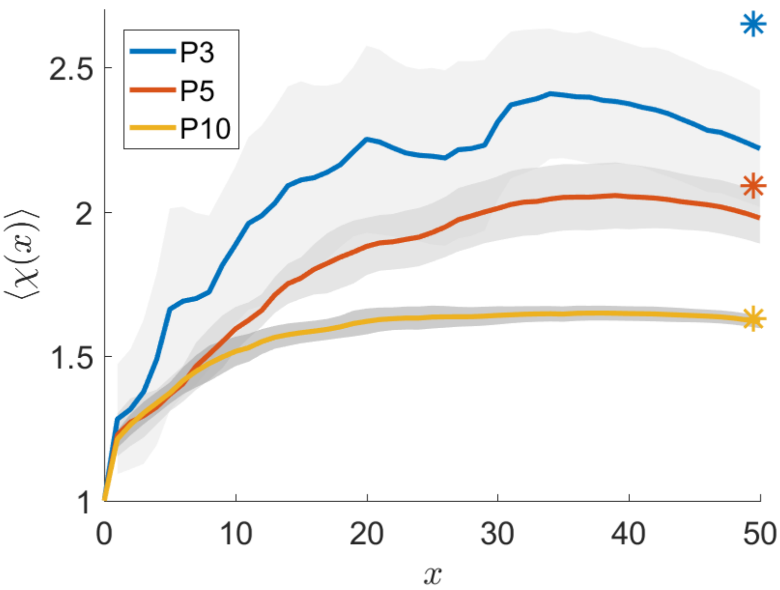

Figure 3. The mean tortuosity calculated as the total travel advective distance divided by the total linear x distance traveled. As network density increases, mean particle trajectories become less tortuous because the denser network probabalistically directs them in direction of primary flow. Shaded areas give 95% confidence intervals across the mean. Stars show ergodic tortuosity values calculated from Eulerian flow field.

lower values near the injection plane because the inlet boundary condition directs all flow into the domain, thereby decreasing the presence of negative velocity regimes near the inlet. Once a sufficient distance from the inlet is reached, memory of the boundary effects has sufficiently diminished and the mean tortuosity asymptotically approaches a constant value.

The mean tortuosity at the domain outlet is $\langle\chi(50)\rangle = 2.21, 1.98, 1.62$ for the $P3, P5, P10$ networks respectively. As network density increases, the mean pathline particle travel distance decreases. Such behavior is expected because in denser networks, more flow can align directly with the pressure gradient and such flow paths have lower tortuosity on average. Additionally, in a denser network, particles encounter more fracture intersections, which preferentially directs them to high velocity flow paths aligned with the primary flow direction. As the network density increases, this asymptotic limit is reached more rapidly because network statistics are more spatially homogeneous and large fluctuations in tortuosities become less probable. The stars in Figure 3 show the asymptotic

Eulerian tortuosity values $\chi_\infty = 2.7, 2.1, 1.6$ for the $P3, P5, P10$ networks. Note that as the fracture density increases, the asymptotic Eulerian and Lagrangian values show closer agreement, suggesting, as before, that the sampling volume required for ergodic behavior decreases.

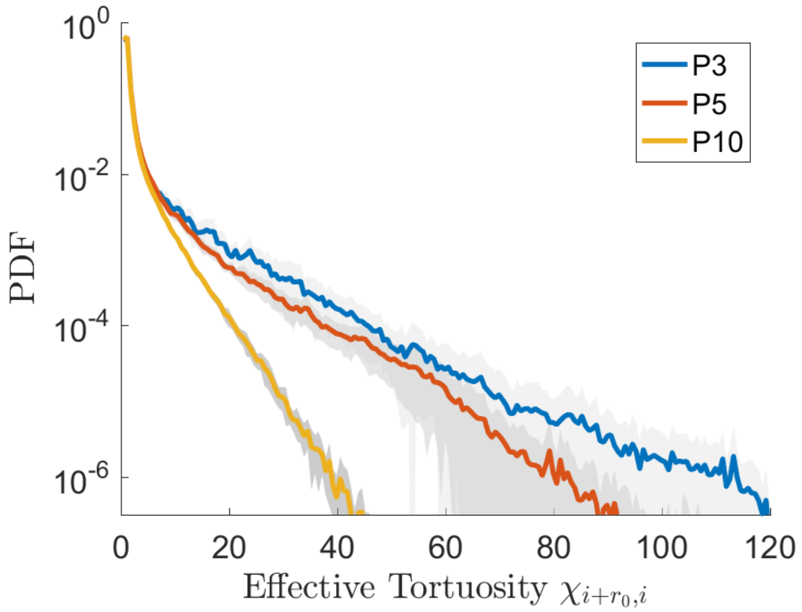

Figure 4. Mean effective tortuosity distributions for the P3 (blue), P5(red) an P10 (yellow) networks. Δl is 2% the entire network length. Effective tortuosity is calculated from the total travel distance between successive control planes. As network density increases, the maximum tortuosity value decreases, because particles in more connected networks encounter more fracture intersections, which preferentially direct particles to flow paths aligned with x and limits highly tortuous paths. Shaded areas show 95% confidence intervals.

Figure 4 shows the effective tortuosity distribution averaged over all network realizations for each network density. The effective tortuosity values can be surprisingly large, with values of $\chi > 50$ for the $P10$ networks and $\chi > 125$ for the $P3$ networks, meaning the total particle travel distance between the first crossings of successive control planes can be up to 2 orders of magnitude larger than the linear x distance. One reason for such large effective χ values is that the 3D topology enables the velocity field to transport particles counter to the mean pressure gradient. These negative velocity regions are important because it enables particle transport in the opposite direction of primary flow and act as a *"trapping"* mechanism, causing long travel times between suc-

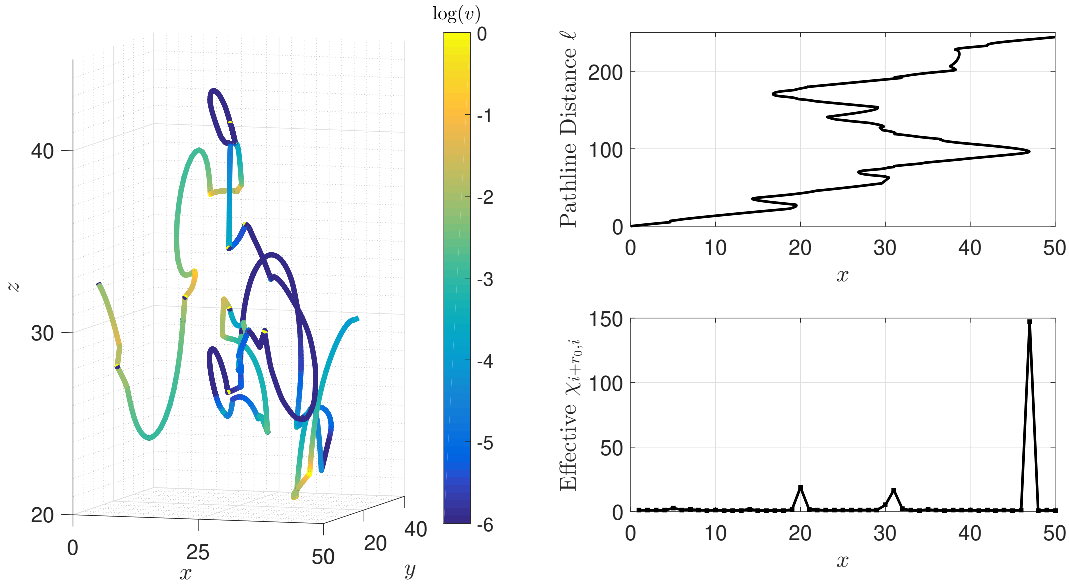

Figure 5. A single sample particle pathline through three dimensional space from a $P3$ network realization is shown on the left. Colors correspond to log of velocity magnitude. This particle trajectory was selected because it displays a highly tortuous pathline. The top right subfigure shows the x coordinate vs total pathline distance for the particle's time series and the bottom right subfigure shows χ values over x with observation windows of size 1.

cessive first crossings of control planes. It is important to note that these large values are partially attributed to how tortuosity is defined here and the size of the sampling window Δl. We refer readers interested in more details related to the wide range of tortuosity definitions to the review by Ghanbarian et al. (2013).

To visually illustrate this, Figure 5 (left) shows a single particle's trajectory through three-dimensional space with colors corresponding to velocity magnitude. The selected particle trajectory is from a P3 network and is chosen specifically as it has one of the highest observed tortuosities. The top right subfigure displays the x coordinate versus total pathline distance for the particle's trajectory and the bottom right subfigure shows the effective tortuosity at each sampled control plane for the same single particle trajectory. Observe that the particle's streamwise position actually may decrease as it advances along the trajectory, demonstrating the presence of a negative velocity zone and resulting in a large local effective tortuosity, $\chi >> 1$. As fracture density increases, the influence of negative velocity zones diminish because particles have increased probability of reaching a fracture intersection and escaping anti-primary flow direction velocity paths. Figure 4 shows that the $P3$ network PDFs have the largest effective χ values and most pronounced tailing behavior, suggesting network density plays an important role in effective tortuosity. Note that although local χ can be very large with maximum effective χ of $140, 150, 51$ for the $P3, P5, P10$ networks respectively, the maximum total $\chi_{50,0}$ are only 5.2, 4.8, 3.2 for the $P3, P5, P10$ networks, demonstrating that localized fracture and flow properties significantly impact domain-scale particle trajectories.

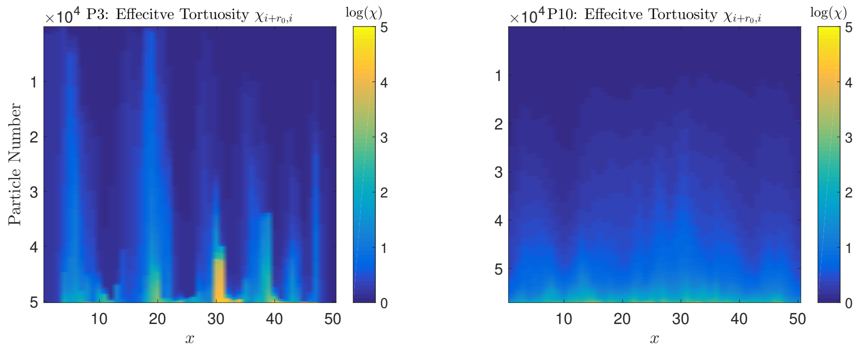

Figure 6. Effective tortuosity for single P3 and P10 realization. Colors correspond to log of tortuosity. Values are sorted from highest to lowest tortuosity. In the P3 network, tortuosity statistics are heavily spatially dependent, and this dependency homogenizes as the network's fracture density increases (right).

To further demonstrate the dependence of local tortuosity on network geometry, we plot local tortuosity through space for every particle in a single realization of a $P3$ network (left) and $P10$ network (right), Figure 6. Colors correspond to the logarithm of local tortuosity values and for each observation window values are sorted from smallest to highest, so that similar tortuosity values are grouped together and appear as bands, i.e. the y axis displays a local tortuosity value for each particle. The banded color structure alternating between dark and light colors in the $P3$ network reflects the network heterogeneity. Dark color bands are regions of the network where nearly all the particles feel effective tortuosity values close to the mean tortuosity. Bright colors are regions of the network where tortuosity values are all larger than the mean. Note that near $\Delta x = 30$ approximately 18% of particles (the orange colored region) experience local tortuosity values greater than 10. This suggests that a significant proportion of particles enter negative velocity/recirculation zones when traversing this particular section of the network and thus its effects should be included in upscaled frameworks, as it delays network scale transport.

The observed effective tortuosity evolution in the $P10$ network (Figure 6) tells a very different story. The increased fracture density of the $P10$ network means Lagrangian statistics across fixed spatial increments are more similar than in the $P3$ network. Therefore, we do not observe as pronounced color bands as in the $P3$ case. Instead, the tortuosity statistics are more spatially homogeneous. This behavior is expected because as the fracture density increases, flow channelization decreases, thereby homogenizing network statistics through space.

3.4 Velocity and Tortuosity

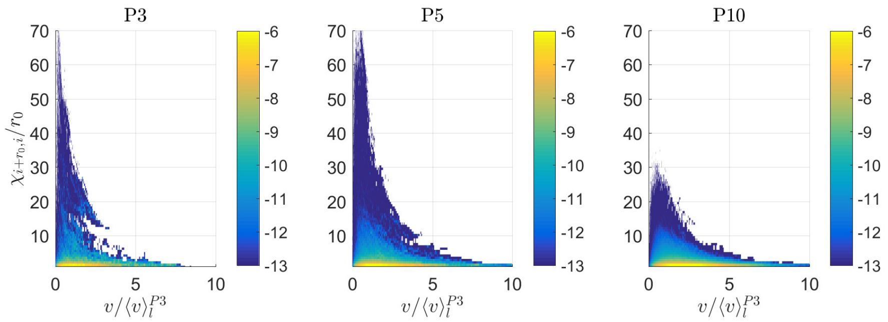

Figure 7. The joint distribution of effective local velocity and tortuosity averaged over all network realizations. Colors correspond to log probabilities. In all network densities, faster velocities have smaller tortuosities. As velocity decreases, the distribution of effective tortuosity widens.

We investigate the relationship between local effective tortuosity and particle velocity. Figure 7 shows joint velocity-tortuosity PDFs averaged over all network realizations for each network density. Note here that velocity corresponds to an effective velocity in the direction of primary flow, i.e. the pathline distance traveled between successive control planes divided by the corresponding transition time. For all network densities, particles with high velocities have small tortuosity values. This is expected because a lower χ means that a particle's advective distance is relatively small, thereby decreasing the time required to travel a fixed x-increment. Additionally for all network densities, the distribution width of local tortuosity values increases with decreasing velocity. Again, this is expected because it takes particles a relatively longer time to travel relatively longer distances, thereby causing lower effective velocities for high χ values. Note the majority of particle tortuosities, even at low velocities are close to the mean tortuosity value (observed as the yellow band near $\chi = 1$). However, there also exists large tortuosity values $\chi > 10$ with relatively slow velocities $v/\langle v \rangle_l^{P3} < 1$. Particles with these slow velocity - high tortuosity pairings produce large travel times that can be orders of magnitude larger than the mean travel time. We hypothesize that these pairings manifest as late time tailing observed on breakthrough curves and therefore must be accounted for in upscaled transport modeling frameworks, i.e. a mean tortuosity value does not effectively represent this velocity-tortuosity correlation structure.

3.5 Breakthrough Curves

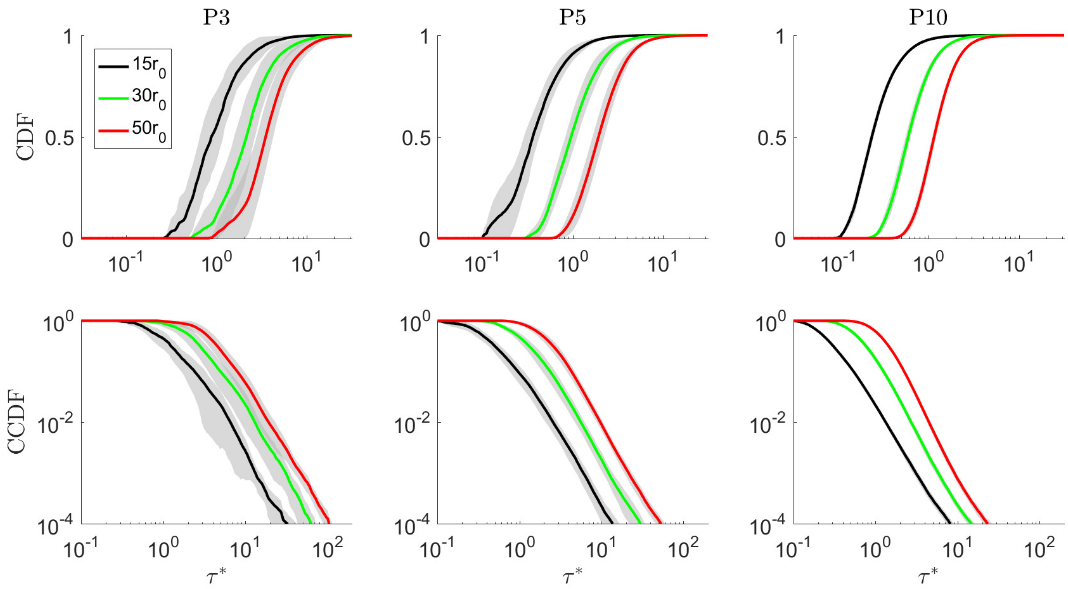

Figure 8. The top row shows mean CDF breakthrough curves at 15 (black), 30 (green), 50 (red) for the $P3, P5, P10$ networks. The gray shade shows 95% confidence intervals across realizations. The bottom row shows mean complementary CDFs, highlighting late time breakthrough behavior.

We inject solute into the domain with a flux-weighted pulse injection at the inlet of each network realization and breakthrough time for each particle is measured at each control plane. Figure 8 shows the mean breakthrough curves for each network density at three control planes $15, 30, 50$. The top row shows cumulative distributions (CDF) of breakthrough times and the bottom rows shows the complementary cumulative distribution function (CCDF), which highlights tailing behavior. As the fracture density increases, mean breakthrough time decreases, which is consistent with the increased mean velocity observed in Eulerian and Lagrangian velocity fields. Furthermore, as the fracture density increases, the uncertainty among network realizations for a given density decreases, shown by a decrease in the 95% confidence intervals (gray). This again demonstrates that Lagrangian statistics homogenize as the network density increases and ergodic assumptions become more valid.

4 Bernoulli Continuous Time Random Walk (CTRW)

Here we introduce a Bernoulli CTRW upscaled model, which is used to predict transport behavior. Bernoulli predictions are compared and validated with the DFNWORKS high fidelity simulations. In this study, we parameterize the Bernoulli CTRW by sampling the Lagrangian velocity magnitudes for all particles at control planes spaced $\Delta l = 1$ in the x-direction. The particle velocity distribution $\psi_l(v)$ corresponds to velocities along particle pathlines and not the x-directional velocity. In such a framework, pathline distances are considered via a tortuosity parameter χ, which typically has been assumed as constant over the entire network (J. Hyman et al., 2019; Kang et al., 2019). Local effective tortuosities, however, are broadly distributed in the studied fracture networks and it remains unanswered whether accounting for this distribution affects model prediction capabilities. Here, we compare predictions of a Bernoulli CTRW with a fixed χ, as typically done in past literature, with those provided by a modified-Bernoulli CTRW that considers the global distribution of χ values.

Effective particle transport through fracture networks is modeled with a Bernoulli CTRW. Like other CTRWs, at each model step particles jump a fixed distance Δl in the x-direction with velocity v, which is sampled from a distribution $\psi_l(v)$. Hence, particle motion through time and space is characterized with a Langevin equation:

$$x_{n+1} = x_n + \Delta l \qquad\qquad t_{n+1} = t_n + \frac{\Delta l}{v_{n+1}} \tag{20}$$

The Bernoulli CTRW framework assumes that Lagrangian velocity evolves at a constant spatial rate, thereby imposing velocity correlation on particle motion. Specifically, a Bernoulli process dictates particle velocity transitions; a particle at model step $n+1$ will continue with its velocity from the previous step n with probability P or sample a new velocity from a global velocity distribution $\psi_l(v)$ with probability $1 - P$. Velocity for particle i at model step $n+1$ is determined as follows:

$$v_{n+1}^i = \begin{cases} v_n^i & P \\ \psi_l(v) & 1-P \end{cases} \tag{21}$$

In this study P can be thought of as the probability that a particles remains on the same fracture over distance Δl, which can be calculated from particle trajectory data. Let there be M control planes perpendicular to the primary flow direction and equally spaced by Δl. Then P is defined as:

$$P = \langle \frac{1}{M} \sum_{m=1}^{M} I_{f_{m+1}=f_m} \rangle, \tag{22}$$

where f denotes the fracture id, I is an indicator function that returns unity if a particle persists on the same fracture over successive control planes, and the angle brackets denote the average over the entire particle plume. In fracture network systems, a particle's current velocity is closely related to the local fracture, and transitioning fractures can result in abrupt particle acceleration, suggesting that setting $1-P$ equal to the probability of changing fractures is appropriate for a Bernoulli framework. The fracture persistent probability P values for a $\Delta l = 1$ are 0.79, 0.77, and 0.75, for $P3, P5$, and $P10$ networks respectively. An equivalent P can be recovered from the Eulerian flow field and network structure.

4.1 Fixed χ Bernoulli

The simplest Bernoulli CTRW framework considered assumes that tortuosity for each particle jump is constant. A tortuosity parameter accounts for mean pathline distance, which effectively increases the travel time of each particle jump in the Langevin time equation (20):

$$t_{n+1} = t_n + \frac{\langle \chi \rangle \Delta l}{v_{n+1}} \tag{23}$$

Here, the mean tortuosity $\langle \chi \rangle = \langle \chi_{50,0} \rangle$, i.e. the mean total advective tortuosity measured at the network outlet. Therefore, at every model step, all particles travel the same distance $\langle \chi \rangle \Delta l$, but travel at different velocities which are sampled from equation 21. The mean tortuosity averaged over all realizations is $\langle \chi \rangle = 2.21, 1.98, 1.62$ for the $P3, P5, P10$ networks respectively. This mean tortuosity Bernoulli CTRW framework acts as a benchmark model upon which we build.

4.2 Random χ Bernoulli

As discussed in §3.3, the network geometry and presence of negative velocity zones means that local particle pathline distances follow a broad distribution spanning orders of magnitude. Therefore, when the local tortuosity differs greatly from the mean tortuosity, travel times may not be accurately represented. We modify the Bernoulli CTRW travel time equation to consider the broad χ distribution:

$$t_{n+1} = t_n + \frac{\chi_n \Delta l}{v_{n+1}}, \quad \chi_n \in \psi(\chi) \tag{24}$$

where χ_n is a random sample from $\psi(\chi)$, the global effective tortuosity distribution for each network realization. $\psi(\chi)$ is found by calculating the total pathline distance of each particle over successive equally spaced control planes of Δl. At each model step and for every particle, we sample a separate velocity according to (21). The corresponding travel time for that step depends on both the velocity and tortuosity. Note that when a velocity persists over multiple model steps, the corresponding χ values are re-sampled and therefore independent of velocity.

4.3 Correlated χ Bernoulli

Finally, we modify the Bernoulli framework to consider the correlation structure between local velocity and local tortuosity. As observed in Figure 7, the effective velocity is highly correlated to the effective tortuosity. High velocities typically have local tortuosity values less than or equal to the mean, while slower velocities have a wide distribution of possible tortuosity values. Naturally, the largest travel times for a particle jump occurs when the velocity is slow and the effective tortuosity is large. We account for this correlation structure by conditioning tortuosity on particle velocity:

$$t_{n+1} = t_n + \frac{\chi_{n+1} \Delta l}{v_{n+1}}, \quad \chi_n \in \psi(\chi | v_n) \tag{25}$$

To condition the local tortuosity on velocity in a discrete framework, we divide the velocity distribution into classes. In this study 100 logarithmically spaced classes, spanning 6 orders of magnitude, are used. Each velocity class has a corresponding distribution of effective tortuosity values, which is determined from the joint velocity-tortuosity pdf in Figure 7. We calculate this joint pdf by generating a velocity-tortuosity pair every time a particle crosses a control plane. The effective velocity for a particle is calculated as $\Delta l / \Delta \tau$, where $\Delta \tau$ is the elapsed time between successive control plane first passage times; the effective tortuosity is then determined from the total advective travel distance Δl in lapsed time Δt, $\chi = \Delta \ell / \Delta l$. Each measured velocity, and therefore also tortuosity, is then binned by velocity class. At every model step we sample a particle velocity, as done in the other Bernoulli frameworks. This sampled velocity is binned and then an effective tortuosity from that same class is sampled. If the velocity of a particle persists from the previous model step, we still sample a new tortuosity value. Note that we sample from the point Lagrangian velocity distribution, not the effective velocity shown in Figure 7, and therefore assume the effective and point velocities share the same correlation structure with tortuosity.

5 Results and Discussion

The role of tortuosity in a Bernoulli CTRW model framework is explored by comparing predicted breakthrough curves with the high fidelity dfnWorks simulations. For each network realization the Bernoulli CTRW and dfnWorks represents the solute plume with the same number of particles. Bernoulli CTRWs are initialized with the inlet flux weighted Lagrangian velocity distribution. The three variants of the Bernoulli framework, fixed χ, randomly sampled χ, and velocity correlated χ, are all tested. We parameterize the Bernoulli models with the point Lagrangian velocity distribution $\psi_l(v)$ and the effective χ distribution $\psi(\chi)$. Control planes are spaced at distance increments of $\Delta l = 1$ and perpendicular to the primary flow direction. We predict breakthrough curves at $15, 30$ and 50. We report our findings in non-dimensional form, where length is relative to r_0, the minimum fracture length, and time is relative to $\tau^* = 50/\langle v \rangle_l^{P3}$, the time to traverse the network if traveling at the mean P3 Lagrangian velocity.

5.1 Breakthrough Curves

Figure 9 shows Bernoulli CTRW breakthrough curve predictions, averaged over all $P5$ network realizations, at three downstream control planes $15, 30$ and 50. The three Bernoulli models, fixed χ (blue), random χ (green), and velocity correlated χ (red) are compared with the dfnWorks measured values (black dots). Notice that the mean χ framework under-predicts concentration at earlier times (CDF < 0.5) at all distances. Sampling randomly from $\psi(\chi)$ shifts the breakthrough curves left and correlating velocity and χ causes a further shift left, meaning increased concentration at earlier times. Such a shift occurs because sampling from a χ distributions allows particle travel dis-

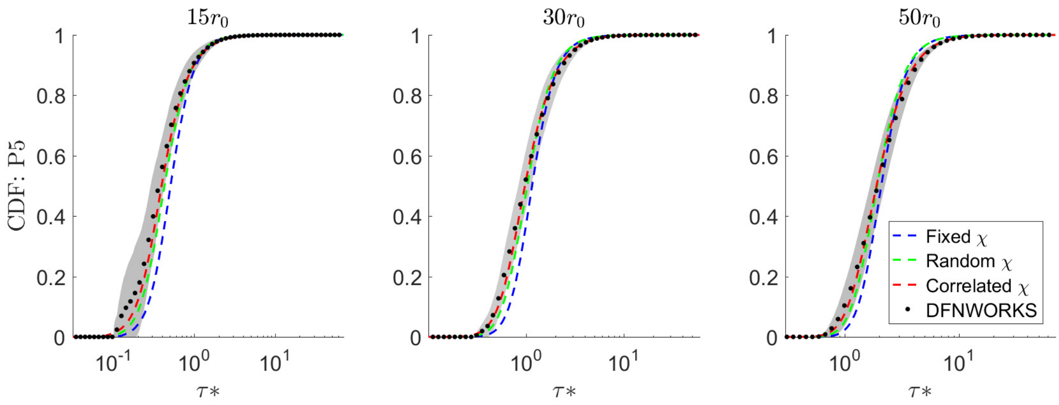

Figure 9. Mean BTC for P5 networks. DFNWORKS -black, classic Bernoulli - blue, Random Tortuosity Bernoulli-green, Velocity-Tortuosity correlated Benroulli-red. Introducing random tortuosity decreases peak arrival time because particles now sample tortuosities less than the mean. Similarly, tailing is slightly increased because we now sample high tortuosities, which leads to larger breakthrough times. Correlating velocity with tortuosity further increases concentration of early arrivals, as fast particles now probablistically sample tortuosities less than the mean. Tailing increases because slow particles have increased probability of sampling high tortuosities resulting in larger breakthrough times. 95% confidence intervals for DFNWORKS are in gray.

tances to be less than the mean χ, thereby enabling particles to travel less distance for breakthrough and increasing concentration at early times. Furthermore, correlating velocity with χ preferentially pairs fast velocities with small χ values, which again results in faster arrival times and increases concentration at early times, compared with the mean χ framework. At distance 15, the correlated χ model best captures early time arrival; all the Bernoulli frameworks sufficiently capture the bend in the CDF observed near CDF values in range [0.8,1]. For a distance 50, the correlated χ framework again best captures early time arrival and most accurately portrays the observed bending behavior for CDF values in the range $[0.8, 1]$.

Model performance is also assessed through breakthrough curve tailing analysis. Figure 10 displays complementary cumulative distribution functions (CCDFs) for all tested Bernoulli frameworks: CCDFs are shown at 15 (black), 30 (green) and 50 (red) for DFNWORKS (dots) and the Bernoulli frameworks (solid lines). The mean and random χ frameworks both underestimate tailing at $x = 30$ and $x = 50$, while sufficiently capturing tailing for $x = 15$, which is consistent with the CDF observations. The opposite is true

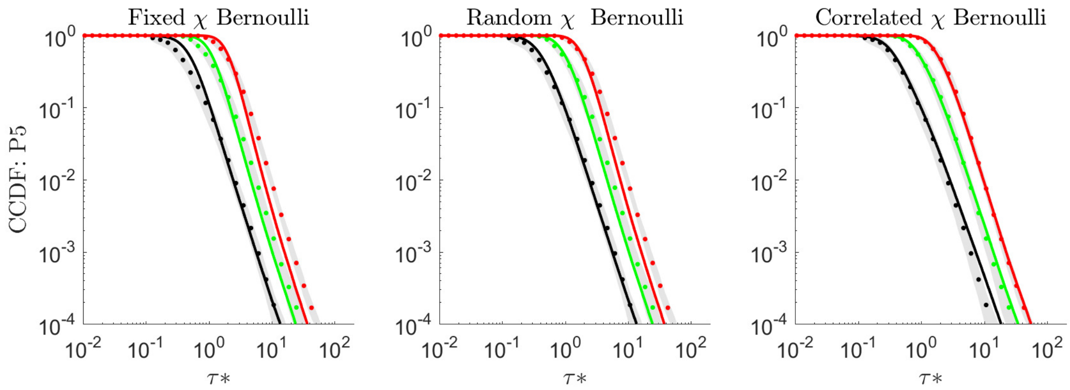

Figure 10. The mean CCDF for P5 for the fixed χ, random χ, and correlated χ Bernoulli models. Dots are DFNWORKS, solid lines are CTRW predictions. CCDF are shown 15 (black), 30 (green), and 50 (red) from the inlet. The correlated tortuosity formulation provides best predictions of tailing behavior at 50 because slow velocity-high tortuosity paths are accounted for.

for the correlated χ framework, where it accurately predicts tailing at distance 30 and 50, but overpredicts tailing at 15. The correlated χ framework overestimates tailing at $x = 15$ because the tortuosity distribution has yet to be fully developed, as demonstrated in Figure 3 which shows that at $x = 15$ mean tortuosity has yet to reach an asymptotic limit. The correlated χ framework samples from the global $\psi(\chi|v)$, meaning that the slowest velocity - largest tortuosity value pairs can be selected at any distance, even though they have yet to occur in the DFNWORKS simulation at this distance. These pairs generate large travel times, which cause an overestimation of tailing behavior at distances near the inlet, where such pairs have yet to be realized. However, by $x = 30$, the mean tortuosity has asymptotically leveled off, and the tailing predictions of the correlated χ framework improve because large travel times have been realized in the network, i.e. the ergodic assumption has become valid.

The observed model performance suggests that negative velocity and stagnation zones must be accurately captured in the Bernoulli framework for proper representation of tailing. Such behavior is represented by correlating velocity and χ, because a non insignificant number of particles traverse large distances at slow velocities, which generate large travel times that affect late time tailing that is only captured if the velocity - tortuosity correlation structure is imposed. Predictions from the random χ framework do not capture this late time tailing, demonstrating that simply considering the full tortuosity distribution alone is insufficient as it does not account for the correlation structure.

5.2 The Role of Fracture Density on Bernoulli CTRW Predictions

We investigate the role of fracture density within a network on solute transport. The role of fracture denisty is assessed via analysis of breakthrough curves, particle total advective travel distances, and particle spreading. We compare Bernoulli CTRW predictions with observations from DFNWORKS simulations. CTRW predictions for different network densities are quantitatively assessed with a Kullback-Leibler error metric.

5.2.1 Comparison of Bernoulli Model Predictions

In BTC predictions, we observe the same trends discussed previously for the $P3$ and $P10$ networks, that is sampling $\psi(\chi)$ increases concentration at early times and sampling $\psi(\chi|v)$ increases concentration at both early and late times relative the other tested frameworks. Figure 11 displays mean breakthrough curve predictions at $x = 50$ for the $P3$ and $P10$ cases. In the sparsest $P3$ networks, it is not obvious which Bernoulli framework offers the best prediction capability, as they all are qualitatively similar. As fracture density decreases, the network's spatial heterogeneity increases and the ergodic assumption upon which the Bernoulli model is built becomes less valid. As a result the importance of accounting for tortuosity as we do also lessens. When fracture density increases such as in the $P10$ cases, the global tortuosity distribution becomes representative of the local distribution because the velocity and network statistics across space homogenize. Consequently, sampling from a χ distribution in the Bernoulli frameworks enhances breakthrough curve predictive capability and correlating χ with velocity further increases model accuracy at both late and early times.

5.2.2 Advective Distance Distribution

The impact of fracture density is further assessed by comparing the distribution of total advective travel distance measured in DFNWORKS with predictions made by the modified Bernoulli frameworks; note $\lambda(x_{50}; \mathbf{a})$ gives particle pathline distances from network inlet to outlet. Such a prediction was not possible in the previous fixed χ frame-

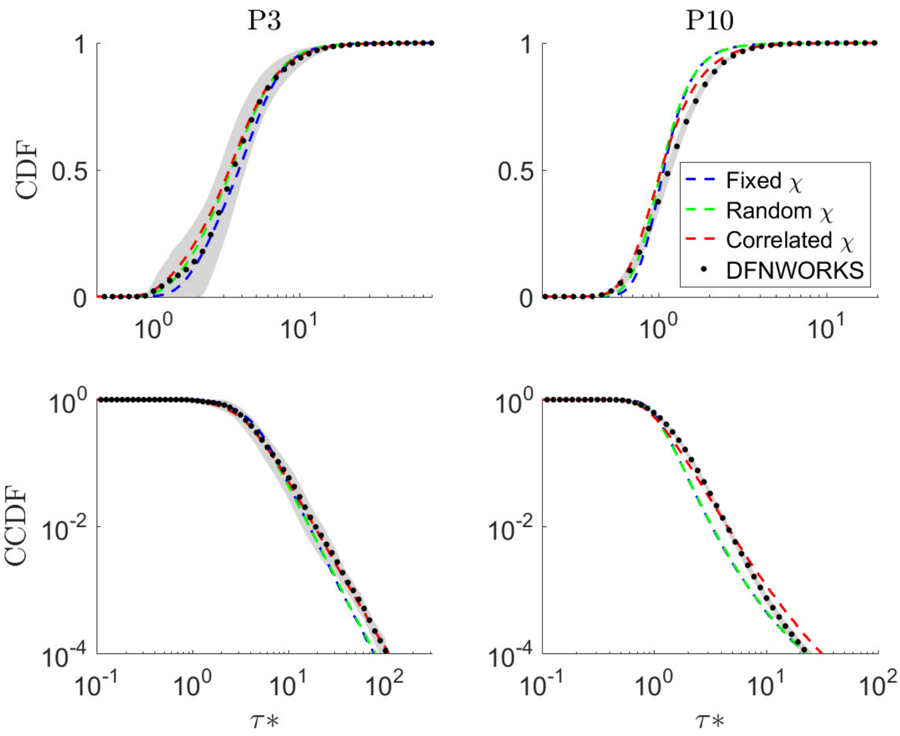

Figure 11. Mean CDF and CCDF BTC for P3 and P10 networks at $x = 50$ for DFNWORKS -black, fixed χ Bernoulli - blue, Random χ Bernoulli-green, correlated χ Benroulli-red. Introducing random tortuosity shifts arrival times left because particles now sample tortuosities less than the mean. Similarly, tailing is slightly increased because we now sample high tortuosities, which leads to larger breakthrough times. Correlating velocity with tortuosity further increases concentration of early arrivals, as fast particles now preferentially sample tortuosities less than the mean. 95% confidence intervals for DFNWORKS are shown in gray.

work because every particle travels the same distance after n model steps, $\lambda(x_n) = n\langle\chi\rangle\Delta l$. Figure 12 shows the travel distance distributions at $x = 50$.

As the fracture density within the network increases, the variance and mean of the observed total advective distance distribution decreases, as well as the variation among network realizations. Increasing the fracture density reduces flow channelization, meaning particles sample more fractures and their respective trajectories homogenize. As a result, the Bernoulli models better predict the distance distribution in denser networks, as sampling effective tortuosities exhibit decreased variance across space. Additionally, we observe that skewness of the distribution decreases in denser networks and the mean

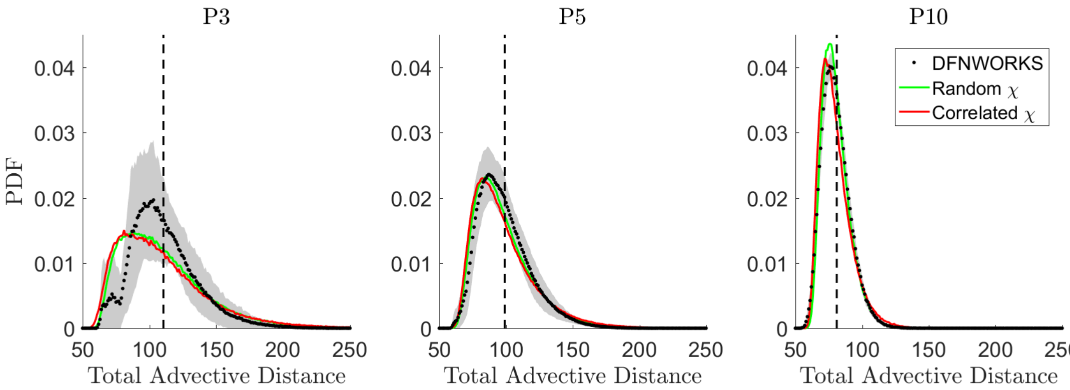

Figure 12. The total advective travel distance $[\lambda(x_{50}; \mathbf{a})]$ distribution at the domain outlet $x = 50$ for DFNWORKS (black), the random χ Bernoulli model (green), and correlated χ Bernoulli model (red). The dashed black line represents the total particle travel distance for a mean χ Bernoulli framework. 95% confidence intervals for DFNWORKS are shown in gray.

tortuosity more closely aligns with the peak value. This suggests that using a mean tortuosity model becomes more reasonable for representing advective travel distances in very dense networks.

In the sparse $P3$ networks, the total advective distance distribution is not accurately predicted because the network topology has an increased role on particle trajectories, and this topology is not properly represented with the proposed Bernoulli frameworks. In these sparse networks, single large fractures have a significant influence on transport; particles tend to persist on these large fractures for longer distances than in the denser networks because they encounter less fracture intersections. Therefore, the orientation of these preferential fractures significantly impacts particle travel distances, and local effective tortuosities for particles on these fractures remains relatively constant over the fracture scale. The proposed Bernoulli frameworks do not account for this spatial correlation structure of tortuosity and thus fail to accurately predict the travel distance distributions.

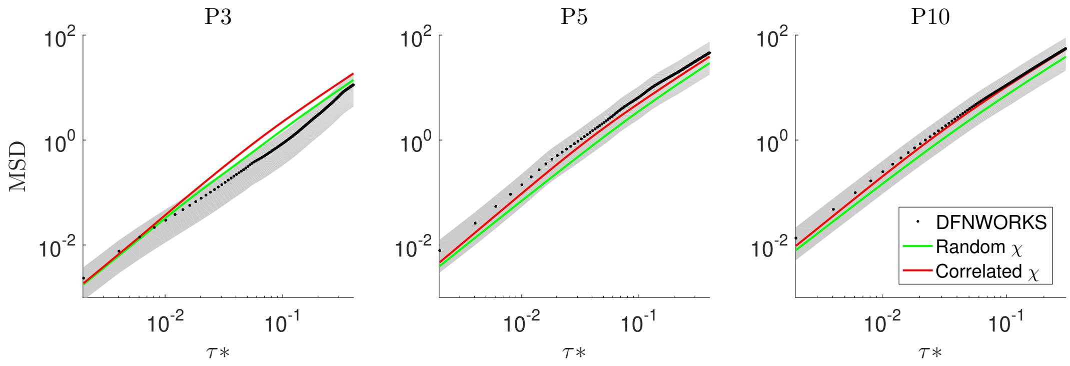

Figure 13. The averaged Mean Square Displacement (MSD) for the random χ (green) and correlated χ (red) Bernoulli models are compared with DFNWORKS simulations (black). Gray shaded region shows 95% confidence intervals of DFNWORKS.

5.2.3 Mean Square Displacement

We study particle spreading in the longitudinal direction with mean square displacement (MSD).

$$MSD(t) = \frac{1}{N}\sum_{i=1}^{N}[x_i(t) - \langle x(t)\rangle]^2 \tag{26}$$

with N being the total number of particles. Figure 13 compares predicted MSD from the Bernoulli models with DFNWORKS simulations. Naturally, the plume spreads over time as the network's topology and corresponding flow field cause particles to experience a wide range of velocities, thereby stretching the plume. Spreading is enhanced in dense networks where the many fractures and intersections create a more dispersed flow field, allowing the solute plume to easily spread in all spatial directions. Notice that there exists two spreading regimes in the P5 and P10 networks, with a break in MSD slope occurring near $\tau^* = 0.03$. At early times ($\tau^* < 0.03$) MSD $\sim t^{1.7}$. Then at later times ($\tau^* > 0.03$) the spreading rate decreases and MSD $\sim t^{1.5}$. A particle traveling at the mean velocity for time $\tau^* = 0.03$ will traverse a distance of approximately 2 and 3 for the P5, P10 networks, which is similar to the mean fracture radius of 1.9. This suggests early solute spreading is controlled by single fractures that intersect the domain inlet, and once solute has traveled a sufficient distance and transitioned from the inlet fractures, network-scale topology plays an increasing role in solute spreading. Note that in the P3 networks, MSD is much more variable across realizations and spreading is controlled by single large fractures which dominate transport behavior and therefore a break in MSD slope is not clearly observed.

We predict MSD with the Bernoulli models and find the same repeating trend; the Bernoulli predictions are very accurate in dense networks and model performance significantly decreases in the sparse P3 networks. In the sparsest networks, the network structure drives transport. This structure is highly heterogeneous and the Bernoulli framework, built on the assumption of ergodicity, does not effectively represent this heterogeneity at earlier times, causing the model to fail. When the fracture density increases, the network statistics homogenize and can be effectively represented with a tortuosity distribution. Note that the correlated χ Bernoulli framework predicts enhanced spreading relative to the random χ framework. The correlated χ preferentially pairs fast velocity with low tortuosity and slow velocity with high tortuosity, meaning fast particles advect downstream very quickly relative to slow particles. This discrepancy in velocities stretches the plume, leading to a higher MSD. This behavior is probabilisticaly less likely with the random χ framework because the velocity-tortuosity correlation is not considered; therefore MSD is lower.

Note that MSD behavior is predicted with a Bernoulli model with a reduced jump size $\Delta l = 1/10$ instead of $\Delta l = 1$, as done with other figures. Smaller jump sizes enable solute spreading to be estimated at earlier times.

5.2.4 Error Metric: Kullback-Leibler

We more formally evaluate the performance of each Bernoulli framework through the Kullback-Leibler divergence. This metric quantifies the similarity between two PDFs, i.e. breakthrough curves in pdf form. The Kullback-Leibler is defined as follows:

$$D_{KL} = \int_{-\infty}^{\infty} p(t) \log\left(\frac{p(t)}{q(t)}\right) dt. \tag{27}$$

Here $p(t)$ and $q(t)$ corresponds with the dfnWorks and Bernoulli CTRW breakthrough curves, respectively. Note that $D_{KL} = 0$ when two PDFs are identical and increases as the expectation of the logarithmic difference increases. We calculate D_{KL} for each network realization at $x = 15, 30, 50$.

Figure 14 shows D_{KL}, averaged over all realizations, at the different control planes. Colors correspond to the three Bernoulli frameworks, fixed χ (black), random χ (green), and correlated χ (red). Shapes identify the three network densities, $P3$ (circles), $P5$ (squares), and $P10$ (triangles). First notice that for the $P5$ and $P10$ networks, red is always below green, which is always below black, meaning that the correlated and random χ frame-

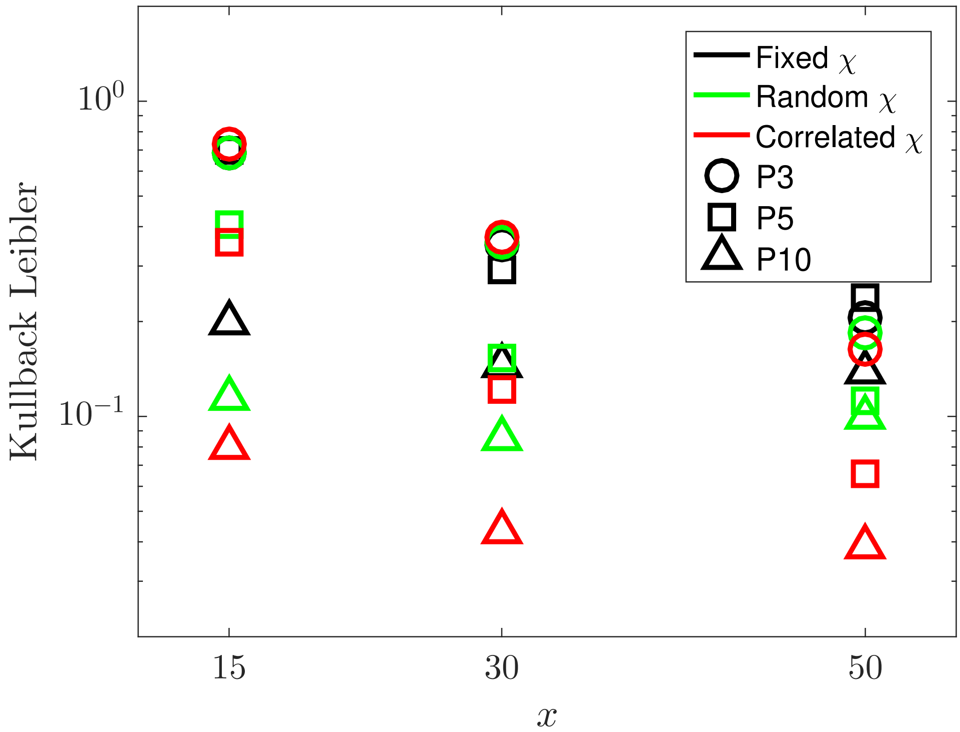

Figure 14. The mean Kullback-Leibler metric for each Bernoulli method; fixed χ (black), random χ (green), and correlated χ (red) for each network realization; P3 (circle), P5 (square), and P10 (triangle). At all distances, the random χ frameworks improves upon the fixed χ Bernoulli. For P5 and P10 networks, the correlated Bernoulli is the best predictive model at all distances. For the P3 network, all Bernoulli frameworks are similar.

work always outperform the fixed χ framework, and the correlated χ framework has the strongest predictive capability. In the $P3$ case, all model performance is nearly identical at distance 15 and 30, with the correlated χ interestingly having slightly higher error when compared with the other frameworks. As noted previously, the correlated χ decreased performance is related to the spatial dependency of tortuosity statistics, meaning that the ergodic assumption is not valid. Once the statistics have fully evolved to the global distribution at distance 50, the correlated χ model outperforms the other models, which is expected since the full global distribution is now equivalent to the sample distribution.

A few general trends become apparent upon further examination of Figure 14.

- As the distance from the injection plane increases, the Bernoulli model performance improves. For each realization, the Bernoulli CTRW is parameterized with the global Lagrangian velocity PDF, meaning that at the exit control plane, particles in DFN-WORKS have fully sampled the entire velocity distribution used to parameterize the model. At upstream control planes, the global pdf has yet to be realized, thereby decreasing predictive accuracy as the distribution becomes more spatially dependent.
- Bernoulli model predictions improve as network density increase. Decreasing network density makes Lagrangian statistics more spatially variant, as was observed in Figure 6. Hence if the local Largangian statistics significantly differ from the global statistics, the model prediction accuracy suffers.

These two trends indicate that Lagrangian ergodicity occurs in fracture networks after the solute plume travels a sufficient distance from the solute source and this distance decreases with increasing fracture density. Once the ergodicity assumption holds, the Bernoulli CTRW model predictions will improve if the tortuosity distribution and tortuosity-velocity correlation structure is considered.

5.3 Larger Scale Breakthrough Curve Predictions

We investigate the role of tortuosity on transport behavior at larger scales by predicting breakthrough curves at $x = 100, 1000$ for each network realization and for each Bernoulli framework considered. A benefit of the Bernoulli CTRW framework is that large scale transport behavior can be predicted at significantly reduced computational costs relative to a DFN model. Given the large scales considered in this section and associated computational resources, DFNWORKS simulations are run in a domain with lengths of 50 (the same ones as previously discussed) and the corresponding statistics are used to parameterize the Bernoulli models. This procedure assumes all fracture length scales that influence large scale transport are represented in the high fidelity domain with length 50.

Figure 15 displays the predicted mean CDF and CCDFs for each network density and for each Bernoulli model. The first important trend that emerges is 1) the fixed and random χ Bernoulli framework predictions converge for all arrival times. At the length scales considered here, the random χ Bernoulli model has sufficiently sampled the tor-

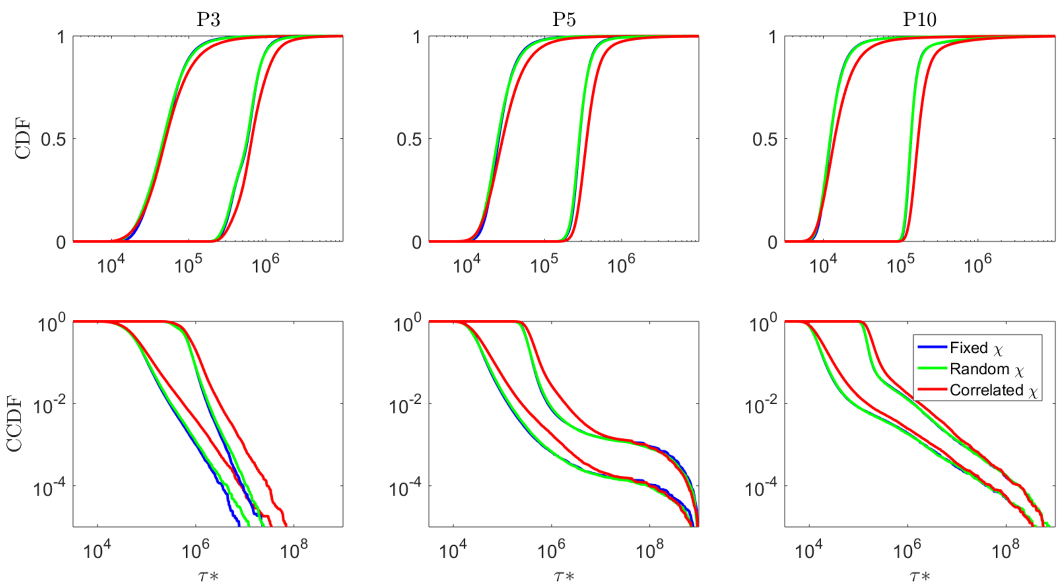

Figure 15. The mean CDF and CCDF breakthrough curves at $x = 100, 1000$ predicted by each the fixed χ (blue), random χ (green), and correlated χ (red) Bernoulli CTRW. The fixed and random χ frameworks converge at large distances. The correlated χ predictions display enhanced tailing and a delayed arrival of peak breakthrough.

tuosity and velocity distributions such that the predicted particle trajectories are approximately equal to those predicted when only considering a fixed tortuosity. This suggests that randomly sampling χ does not improve breakthrough curve predictions at large distances, once the χ distribution has undergone sufficient sampling. Previous studies have focused on fixed χ Bernoulli models, which are suitable when velocity and tortuosity are independent and predictions are made for distances where the solute plume has fully sampled the tortuosity distribution. These assumptions are violated for the scales of interest in this study and so a correlated χ framework is considered..

The second important trend is that the correlated χ framework delays mean transport. For all network densities, correlating χ with velocity results in large travel times. As the distance from the injection source increases, particles have increased probability of sampling large travel times generated from low velocity- high χ pairs, which delays mean transport. This delayed transport is especially obvious in the CCDFs, which highlight breakthrough curve tailing behavior at late times. Note enhanced tailing of the correlated tortuosity model is observed for all fracture densities and distances from source.

As the fracture density and the distance from particle source increase, the observed difference in late time tailing decreases, which is expected given that both of these factors homogenize Lagrangian statistics. However, even in the densest networks at the kilometer scale, we still observe significant difference in tailing between the correlated and fixed tortuosity CTRW models at intermediate CCDF values [0.01,1]. Interestingly, the fixed χ CTRW underestimated tailing for this same CCDF regime in the fracture networks studied by (J. Hyman et al., 2019), although their networks had higher density. This again shows that the velocity-tortuosity correlation structure is important for breakthrough tailing, as slow velocity large χ regions delay solute transport. Therefore, parameterization of tortuosity needs to be carefully considered if we are to develop accurate upscaled models, capable of predicting late time behaviors. Treating χ as a fixed value becomes more valid as network density and distance from source increase, but as we see here, may not be valid for many typical scales of study.

6 Discussion

Here, we consider fracture networks of three different densities with radii sampled from a truncated power law distribution and investigate the influence of fracture density on flow and transport. As the fracture density increases flow channelization decreases and network connectivity increases. These changes in flow and topological properties cause significant differences in particle trajectories:

1. As connectivity increases the mean advective travel distance decreases, i.e. χ_∞ decreases, because solute encounters more fracture intersections where they are preferentially directed to high discharge channels which are aligned with the pressure gradient.
2. Local tortuosity statistics become spatially independent as fracture density increases.
3. The distribution of local effective tortuosities χ display greater variance and increased probability for large χ values in sparse networks.
4. Increased flow channelization in sparse networks results in decreased spreading of the solute plume.
5. Increasing the fracture density increases the mean Eulerian velocity magnitude, which in turn decreases the mean particle breakthrough time.

We predict breakthrough curves with a correlated CTRW framework that assumes a spatial Markov process. The traditional spatial Markov model assumes travel time statistics across successive control planes are spatially stationary, which is clearly not satisfied in sparse networks where network topology is spatially variant (Figure 6). Hence we opt to upscale transport via a Bernoulli CTRW framework, which also assumes solute trajectories follow a spatial Markov process, while allowing velocity statistics to evolve from an initial to steady distribution. Past applications of the Bernoulli CTRW framework assume a constant tortuosity parameter at each model step, which effectively delays transport. However we demonstrate that local tortuosity values span a wide distribution and are correlated with velocity. Using this fact, we investigate how relaxing the fixed tortuosity value improves breakthrough curve predictions and better captures the local effects induced by the network structure.

The tortuosity value in the Bernoulli framework is relaxed in two novel ways 1) at every model step local tortuosity is sampled from a global distribution, and 2) at every model step local tortuosity is correlated with the velocity field. Both of these methods allow the distribution of particle distances to be estimated, which was previously not possible in a Bernoulli framework. In both cases, we assume Lagrangian ergodicity, as consistent with the Bernoulli framework, meaning the modified models only will improve model performance if tortuosity distributions are stationary. We find that both methods improve breakthrough curve predictions as quantified with Kullback-Leibler divergence.

Method 1, sampling from an uncorrelated tortuosity distribution, decreases the mean breakthrough time relative to a fixed tortuosity model. Sampling from the global distribution enables particles to have tortuosity values less than the mean, allowing particles to travel less distance and traverse the domain at increased effective velocity values. This framework is thus better suited for capturing early time breakthrough than a mean tortuosity framework. However, large tortuosity values are correlated with low velocities and sampling randomly from a global distribution does not capture this correlation, which is important for tailing behavior.

We account for correlation by modifying the Bernoulli framework to sample from a joint velocity-tortuosity distribution. We show that this framework adequately captures both early and late time tailing of breakthrough curves and offers significant improvement over a mean tortousity Bernoulli framework for the $P5$ and $P10$ networks, where ergodic assumptions are valid, but predictions remain relatively unchanged for the sparse $P3$ networks, where ergodicity may not be valid. Hence, in fractured media transport is a function of the network structure and flow field, and ergodic assumptions (for a fixed control volume) are more reasonable as fracture density increases.

Finally, we use the upscaled CTRW models to predict transport through larger domains, in this case the kilometer scale (which is cost prohibitive with the fully DFN resolved models). We find that at these scales, breakthrough predictions of the random χ and fixed χ frameworks converge because the χ distribution has undergone sufficient sampling, thereby minimizing effects of large χ values. The correlated χ framework, however, predicts enhanced tailing, demonstrating local stagnation zones and areas of negative velocity have an important impact on transport behavior, even at such large scales. This suggests that incorporating the local topological influences of a network must be considered in an upscaled framework for accurate model predictions.

The results of this study demonstrate that local network topology, i.e. tortuosity, is important for network scale transport and we can parameterize such effects in upscaled modeling frameworks. However, in this study such parameterizations were derived from high fidelity models that required Lagrangian particle tracking statistics. How to parameterize the modified Bernoulli models from field observations remains unclear and requires further investigation, although detailed geostatical measures may aid in that regard (Ceriotti et al., 2019). Furthermore, the conclusions of this study are drawn from networks with only three percolation lengths and where fracture radii are sampled from a power law distribution, and so our conclusions may not reflect universal behavior. Despite these considerations, we learn from model predictions that tortuosity plays an important role in transport and by coupling the distribution of network topology statistics with a spatial Markov model, we can faithfully portray transport in the fractured media considered here.

Acknowledgments

TS is supported by the National Science Foundation Graduate Research Fellowship under Grant No. DGE-1841556. DB was supported by the US Army Research Office under Contract/Grant number W911NF-18-1-0338 as well as by the National Science Foundation under award CBET-1803989. Los Alamos National Laboratory is operated by Triad National Security, LLC, for the National Nuclear Security Administration of U.S. Department of Energy (Contract No. 89233218CNA000001). J.D.H. acknowledges support from the LANL LDRD program office Grant Number # 20180621ECR DOE's Office of Science Basic Energy Sciences E3W1: LA-UR-19-27671. MD acknowledges funding from the European Research Council under the European Unions Seventh Framework Programme (FP7/2007-2013)/ ERC Grant Agreement No. 617511 (MHetScale). DFNWORKS can be obtained at https://github.com/lanl/dfnWorks and simulation data can be obtained at https://github.com/tjsherman24/FractureNetworkDensity.

References

Aldrich, G., Hyman, J. D., Karra, S., Gable, C. W., Makedonska, N., Viswanathan, H., ... Hamann, B. (2017). Analysis and visualization of discrete fracture networks using a flow topology graph. *IEEE Transactions on Visualization and Computer Graphics*, *23*(8), 1896–1909. doi: 10.1109/tvcg.2016.2582174

Andresen, C. A., Hansen, A., Le Goc, R., Davy, P., & Hope, S. M. (2013). Topology of fracture networks. *Frontiers in Physics*, *1*, Art–7.

Barbier, E. (2002). Geothermal energy technology and current status: an overview. *Renew. Sust. Energ. Rev.*, *6*(1-2), 3–65.

Becker, M. W., & Shapiro, A. M. (2000). Tracer transport in fractured crystalline rock: Evidence of nondiffusive breakthrough tailing. *Water Resources Research*, *36*(7), 1677–1686.

Becker, M. W., & Shapiro, A. M. (2003). Interpreting tracer breakthrough tailing from different forced-gradient tracer experiment configurations in fractured bedrock. *Water Resources Research*, *39*(1).

Berkowitz, B., & Balberg, I. (1993). Percolation theory and its application to groundwater hydrology. *Water Resources Res*, *29*(4), 775–794.

Berkowitz, B., Cortis, A., Dentz, M., & Scher, H. (2006). Modeling non-Fickian transport in geological formations as a continuous time random walk. *Reviews of Geophysics*, *44*(2), RG2003.

Berkowitz, B., & Scher, H. (1997). Anomalous transport in random fracture networks. *Phys. Rev. Lett.*, *79*(20), 4038–4041.

Bogdanov, I., Mourzenko, V., Thovert, J.-F., & Adler, P. (2007). Effective permeability of fractured porous media with power-law distribution of fracture sizes. *Phys. Rev. E*, *76*(3), 036309.

Bolster, D., Méheust, Y., Le Borgne, T., Bouquain, J., & Davy, P. (2014). Modeling preasymptotic transport in flows with significant inertial and trapping effects–the importance of velocity correlations and a spatial markov model. *Adv. Water Research*, *70*, 89–103.

Bonnet, E., Bour, O., Odling, N. E., Davy, P., Main, I., Cowie, P., & Berkowitz, B. (2001). Scaling of fracture systems in geological media. *Rev. Geophys.*, *39*(3), 347–383.

Bour, O., & Davy, P. (1997). Connectivity of random fault networks following a power law fault length distribution. *Water Resources Research*, *33*(7), 1567–1583.

Bour, O., & Davy, P. (1998). On the connectivity of three-dimensional fault networks. *Water Resources Research*, *34*(10), 2611–2622.

Cacas, M.-C., Ledoux, E., Marsily, G., Tillie, B., Barbreau, A., Durand, E., … Peaudecerf, P. (1990). Modeling fracture flow with a stochastic discrete fracture network: calibration and validation: 1. the flow model. *Water Resources Research*, *26*(3), 479–489.

Carrel, M., Morales, V. L., Dentz, M., Derlon, N., Morgenroth, E., & Holzner, M. (2018). Pore-scale hydrodynamics in a progressively bioclogged three-dimensional porous medium: 3-d particle tracking experiments and stochastic transport modeling. *Water Resources Research*, *54*(3), 2183–2198.

Ceriotti, G., Russian, A., Bolster, D., & Porta, G. (2019). A double-continuum transport model for segregated porous media: Derivation and sensitivity analysis-driven calibration. *Advances in Water Resources*, *128*, 206–217.

Comolli, A., & Dentz, M. (2017). Anomalous dispersion in correlated porous media: a coupled continuous time random walk approach. *Eur. Phys. J. B*, *90*(9), 166.

Cushman, J. H. (2013). *The physics of fluids in hierarchical porous media: Angstroms to miles* (Vol. 10). Springer Science & Business Media.

De Anna, P., Le Borgne, T., Dentz, M., Tartakovsky, A. M., Bolster, D., & Davy, P. (2013). Flow intermittency, dispersion, and correlated continuous time random walks in porous media. *Physical review letters*, *110*(18), 184502.

de Dreuzy, J., Darcel, C., Davy, P., & Bour, O. (2004). Influence of spatial correlation of fracture centers on the permeability of two-dimensional fracture networks following a power law length distribution. *Water Resources Research*, *40*(1).

de Dreuzy, J., Davy, P., & Bour, O. (2000). Percolation threshold of 3d random ellipses with widely-scattered distributions of eccentricity and size. *Phys. Rev. E*, *62*(5), 5948–5952.

de Dreuzy, J., Davy, P., & Bour, O. (2002). Hydraulic properties of two-dimensional random fracture networks following power law distributions of length and aperture. *Water Resources Research*, *38*(12).

de Dreuzy, J., Méheust, Y., & Pichot, G. (2012). Influence of fracture scale heterogeneity on the flow properties of three-dimensional discrete fracture networks. *J. Geophys. Research-Sol. Ea.*, *117*(B11).

Dentz, M., & Bolster, D. (2010). Distribution-versus correlation-induced anomalous transport in quenched random velocity fields. *Phys. Rev. Lett.*, *105*(24), 244301.

Dentz, M., Kang, P. K., Comolli, A., Le Borgne, T., & Lester, D. R. (2016). Continuous time random walks for the evolution of lagrangian velocities. *Physical Review Fluids*, *1*(7), 074004.

Dershowitz, W. S., & Herda, H. H. (1992). Interpretation of fracture spacing and intensity. In *The 33th us symposium on rock mechanics (USRMS).*

Frampton, A., & Cvetkovic, V. (2009). Significance of injection modes and heterogeneity on spatial and temporal dispersion of advecting particles in two-dimensional discrete fracture networks. *Adv. Water Resources*, *32*(5), 649–658.

Frampton, A., & Cvetkovic, V. (2010). Inference of field-scale fracture transmissivities in crystalline rock using flow log measurements. *Water Resources Research*, *46*(11).

Frampton, A., Hyman, J., & Zou, L. (2019). Advective transport in discrete fracture networks with connected and disconnected textures representing internal aperture variability. *Water Resources Research.* Retrieved from `https://agupubs.onlinelibrary.wiley.com/doi/abs/10.1029/2018WR024322` doi: 10.1029/2018WR024322

Ghanbarian, B., Hunt, A. G., Ewing, R. P., & Sahimi, M. (2013). Tortuosity in porous media: a critical review. *Soil science society of America journal*, *77*(5), 1461–1477.

Hakoun, V., Comolli, A., & Dentz, M. (2019). Upscaling and prediction of lagrangian velocity dynamics in heterogeneous porous media. *Water Resources Research*, *55*(5), 3976–3996.

Holzner, M., Morales, V. L., Willmann, M., & Dentz, M. (2015). Intermittent lagrangian velocities and accelerations in three-dimensional porous medium flow. *Physical Review E*, *92*(1), 013015.

Hope, S. M., Davy, P., Maillot, J., Le Goc, R., & Hansen, A. (2015). Topological impact of constrained fracture growth. *Frontiers in Physics*, *3*, 75.

Huseby, O., Thovert, J., & Adler, P. (1997). Geometry and topology of fracture systems. *J. Phys A-Math Gen*, *30*(5), 1415.

Hyman, J., Dentz, M., Hagberg, A., & Kang, P. K. (2019). Linking structural and transport properties in three-dimensional fracture networks. *Journal of Geophysical Research: Solid Earth*.

Hyman, J. D., Aldrich, G., Viswanathan, H., Makedonska, N., & Karra, S. (2016). Fracture size and transmissivity correlations: Implications for transport simulations in sparse three-dimensional discrete fracture networks following a truncated power law distribution of fracture size. *Water Rescour. Research*, *52*(8), 6472–6489. Retrieved from `http://dx.doi.org/10.1002/2016WR018806` doi: 10.1002/2016WR018806

Hyman, J. D., Gable, C. W., Painter, S. L., & Makedonska, N. (2014). Conforming Delaunay triangulation of stochastically generated three dimensional discrete fracture networks: A feature rejection algorithm for meshing strategy. *SIAM J. Sci. Comput.*, *36*(4), A1871–A1894.

Hyman, J. D., Hagberg, A., Osthus, D., Srinivasan, S., Viswanathan, H., & Srinivasan, G. (2018). Identifying backbones in three-dimensional discrete fracture networks: A bipartite graph-based approach. *SIAM Multiscale Modeling and Simulation*.

Hyman, J. D., Hagberg, A., Srinivasan, G., Mohd-Yusof, J., & Viswanathan, H. (2017). Predictions of first passage times in sparse discrete fracture networks using graph-based reductions. *Phys. Rev. E*, *96*(1), 013304. doi:

10.1103/PhysRevE.96.013304

Hyman, J. D., & Jiménez-Martínez, J. (2018). Dispersion and mixing in three-dimensional discrete fracture networks: Nonlinear interplay between structural and hydraulic heterogeneity. *Water Rescour. Research*, *54*(5), 3243-3258.

Hyman, J. D., Jiménez-Martínez, J., Viswanathan, H., Carey, J., Porter, M., Rougier, E., … Makedonska, N. (2016). Understanding hydraulic fracturing: a multi-scale problem. *Phil. Trans. R. Soc. A*, *374*(2078), 20150426.

Hyman, J. D., Karra, S., Makedonska, N., Gable, C. W., Painter, S. L., & Viswanathan, H. S. (2015). dfnWorks: A discrete fracture network framework for modeling subsurface flow and transport. *Comput. Geosci.*, *84*, 10–19.

Hyman, J. D., Painter, S. L., Viswanathan, H., Makedonska, N., & Karra, S. (2015). Influence of injection mode on transport properties in kilometer-scale three-dimensional discrete fracture networks. *Water Resources Research*, *51*(9), 7289–7308.

Joyce, S., Hartley, L., Applegate, D., Hoek, J., & Jackson, P. (2014). Multi-scale groundwater flow modeling during temperate climate conditions for the safety assessment of the proposed high-level nuclear waste repository site at forsmark, sweden. *Hydrogeol. J.*, *22*(6), 1233–1249.

Kang, P. K., Anna, P., Nunes, J. P., Bijeljic, B., Blunt, M. J., & Juanes, R. (2014). Pore-scale intermittent velocity structure underpinning anomalous transport through 3-d porous media. *Geophysical Research Letters*, *41*(17), 6184–6190.

Kang, P. K., Brown, S., & Juanes, R. (2016). Emergence of anomalous transport in stressed rough fractures. *Earth and Planetary Science Letters*, *454*, 46–54.

Kang, P. K., Dentz, M., Le Borgne, T., & Juanes, R. (2011). Spatial markov model of anomalous transport through random lattice networks. *Physical review letters*, *107*(18), 180602.

Kang, P. K., Dentz, M., Le Borgne, T., & Juanes, R. (2015). Anomalous transport on regular fracture networks: Impact of conductivity heterogeneity and mixing at fracture intersections. *Physical Review E*, *92*(2), 022148.

Kang, P. K., Dentz, M., Le Borgne, T., Lee, S., & Juanes, R. (2017). Anomalous transport in disordered fracture networks: spatial Markov model for dispersion with variable injection modes. *Adv. Water Resources*, *106*, 80–94.

Kang, P. K., Le Borgne, T., Dentz, M., Bour, O., & Juanes, R. (2015). Impact of velocity correlation and distribution on transport in fractured media: Field evidence and theoretical model. *Water Resources Research*, *51*(2), 940–959.

Kang, P. K., Lei, Q., Dentz, M., & Juanes, R. (2019). Stress-induced anomalous transport in natural fracture networks. *Water Resources Research*.

Koponen, A., Kataja, M., & Timonen, J. (1996). Tortuous flow in porous media. *Physical Review E*, *54*(1), 406.

Kreft, A., & Zuber, A. (1978). On the physical meaning of the dispersion equation and its solutions for different initial and boundary conditions. *Chem. Eng. Sci.*, *33*, 1471–1480.

LaGriT. (2013). *Los Alamos Grid Toolbox, (LaGriT) Los Alamos National Laboratory.* http://lagrit.lanl.gov.

Le Borgne, T., Dentz, M., & Carrera, J. (2008a). Lagrangian statistical model for transport in highly heterogeneous velocity fields. *Physical review letters*, *101*(9), 090601.

Le Borgne, T., Dentz, M., & Carrera, J. (2008b). Spatial markov processes for modeling lagrangian particle dynamics in heterogeneous porous media. *Physical Review E*, *78*(2), 026308.

Lichtner, P., Hammond, G., Lu, C., Karra, S., Bisht, G., Andre, B., … Kumar, J. (2015). *PFLOTRAN user manual: A massively parallel reactive flow and transport model for describing surface and subsurface processes* (Tech. Rep.). (Report No.: LA-UR-15-20403) Los Alamos National Laboratory.

Maillot, J., Davy, P., Le Goc, R., Darcel, C., & De Dreuzy, J.-R. (2016). Connectivity, permeability, and channeling in randomly distributed and kinematically defined discrete fracture network models. *Water Resources Research*, *52*(11), 8526–8545.

Makedonska, N., Hyman, J. D., Karra, S., Painter, S. L., Gable, C. W. W., & Viswanathan, H. S. (2016). Evaluating the effect of internal aperture variability on transport in kilometer scale discrete fracture networks. *Adv. Water Resources*, *94*, 486–497.

Makedonska, N., Painter, S. L., Bui, Q. M., Gable, C. W., & Karra, S. (2015). Particle tracking approach for transport in three-dimensional discrete fracture networks. *Computat. Geosci.*, 1–15.

Massoudieh, A., Dentz, M., & Alikhani, J. (2017). A spatial markov model for the evolution of the joint distribution of groundwater age, arrival time, and velocity in heterogeneous media. *Water Resources Research*, *53*(7), 5495–5515.

Morales, V. L., Dentz, M., Willmann, M., & Holzner, M. (2017). Stochastic dynamics of intermittent pore-scale particle motion in three-dimensional porous media: Experiments and theory. *Geophysical Research Letters*, *44*(18), 9361–9371.

Mourzenko, V., Thovert, J.-F., & Adler, P. (2005). Percolation of three-dimensional fracture networks with power-law size distribution. *Phys. Rev. E*, *72*(3), 036103.

Newman, M. E. (2002). Assortative mixing in networks. *Phys. Rev. Lett.*, *89*(20), 208701.

Newman, M. E. (2003). Mixing patterns in networks. *Phys. Rev. E*, *67*(2), 026126.

Noetinger, B., Roubinet, D., Russian, A., Le Borgne, T., Delay, F., Dentz, M., ... Gouze, P. (2016). Random walk methods for modeling hydrodynamic transport in porous and fractured media from pore to reservoir scale. *Transp. Porous Media*, 1–41.

Pacala, S., & Socolow, R. (2004). Stabilization wedges: solving the climate problem for the next 50 years with current technologies. *Science*, *305*(5686), 968–972.

Painter, S., & Cvetkovic, V. (2005). Upscaling discrete fracture network simulations: An alternative to continuum transport models. *Water Resources Res*, *41*, W02002.

Painter, S. L., Gable, C. W., & Kelkar, S. (2012). Pathline tracing on fully unstructured control-volume grids. *Computat. Geosci.*, *16*(4), 1125–1134.

Park, Y.-J., Lee, K.-K., Kosakowski, G., & Berkowitz, B. (2003). Transport behavior in three-dimensional fracture intersections. *Water Resources Research*, *39*(8).

Puyguiraud, A., Gouze, P., & Dentz, M. (2019a). Stochastic dynamics of lagrangian pore-scale velocities in three-dimensional porous media. *Water Resources Research*, *55*(2), 1196–1217.

Puyguiraud, A., Gouze, P., & Dentz, M. (2019b, Apr 04). Upscaling of anomalous pore-scale dispersion. *Transport in Porous Media*. Retrieved from `https://doi.org/10.1007/s11242-019-01273-3` doi: 10.1007/s11242-019-01273-3

Rizzo, C. B., & de Barros, F. P. (2017). Minimum hydraulic resistance and least resistance path in heterogeneous porous media. *Water Rescour. Research*, *53*(10), 8596–8613.

Sahimi, M. (1994). *Applications of percolation theory.* CRC Press.

Sherman, T., Fakhari, A., Miller, S., Singha, K., & Bolster, D. (2017). Parameterizing the spatial markov model from breakthrough curve data alone. *Water Resources Research*, *53*(12), 10888–10898.

Sherman, T., Foster, A., Bolster, D., & Singha, K. (2018). Predicting downstream concentration histories from upstream data in column experiments. *Water Resources Research*.

Sherman, T., Hyman, J. D., Bolster, D., Makedonska, N., & Srinivasan, G. (2019). Characterizing the impact of particle behavior at fracture intersections in three-dimensional discrete fracture networks. *Physical Review E*, *99*(1), 013110.

Svensk Kärnbränslehantering AB. (2010). *Data report for the safety assessment SR-site (TR-10-52)* (Tech. Rep.). Svensk Kärnbränslehantering AB.

Valera, M., Guo, Z., Kelly, P., Matz, S., Cantu, V. A., Percus, A. G., ... Viswanathan, H. S. (2018, Jan 24). Machine learning for graph-based representations of three-dimensional discrete fracture networks. *Computat. Geosci.*. Retrieved from https://doi.org/10.1007/s10596-018-9720-1 doi: 10.1007/s10596-018-9720-1

Wellman, T. P., Shapiro, A. M., & Hill, M. C. (2009). Effects of simplifying fracture network representation on inert chemical migration in fracture-controlled aquifers. *Water Resources Research*, *45*(1).

Wood, A. T. (1994). Simulation of the von Mises Fisher distribution. *Commun. Stat. Simulat.*, *23*(1), 157–164.